Master thesis

2D simulation of rf-discharges

Submitted by: Paul Matthias
Born at: 15.05.1990, Greifswald

Reviewer: Prof. Dr. Ralf Schneider
                 Prof. Dr. Jürgen Meichsner

Submitted at: August 6, 2015

Contents

1 Introduction

Reactive plasmas are used in a lot of industrial applications. Especially plasma etching [1] and sputter processes [2] are of high importance, for example for the production of computer chips. Normally, capacitive-coupled discharges with a radio-frequency modulated voltage are used. The advantage is the high ion energy at the target (at the cathode) while having no net current destroying it [3].

The latest results of an experiment with electronegative discharges have shown a high-energy peak of the negative ions arriving at the anode [4] as seen in figure (1.1). This peak depends on the cathode material used. One possible explanation is ionization at or close to the surface for the production of negative ions.
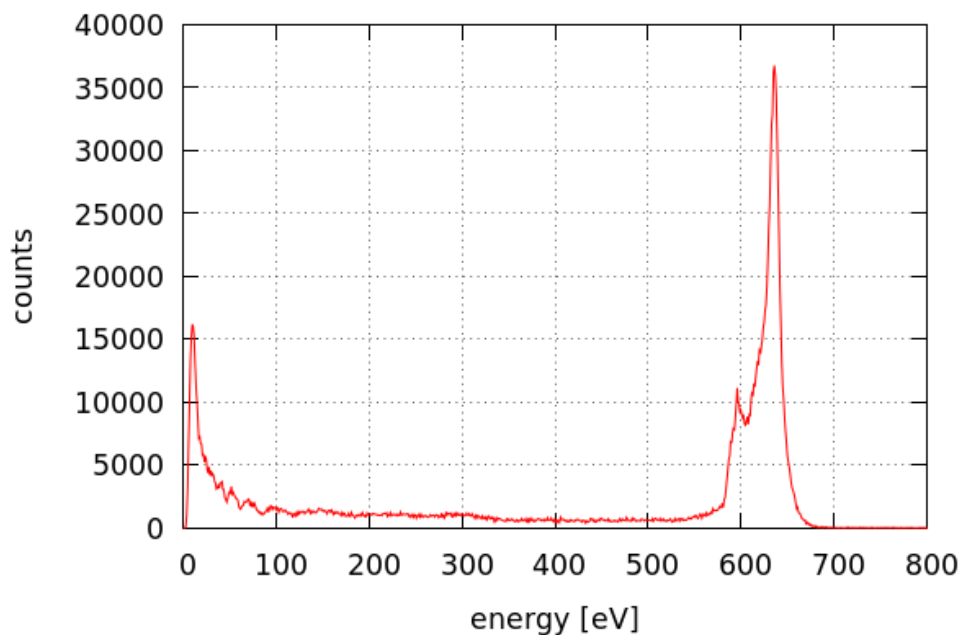
Figure 1.1: Experimental measured negatively charged oxygen ions arriving at the grounded anode as shown in [4]. The cathode material used was Magnesiu-moxide (MgO) and the cathode was powered with 50 W.

Until now a clear understanding of this signature in the distribution function of negative ions measured at the grounded anode is missing. In this thesis I want to improve the insight into microscopic mechanisms of electronegative plasmas and surface ionization effects. Therefore, I will introduce the basics of an asymmetric capacitively coupled radio frequency (ccrf) discharge. Nearly all real discharges are asymmetric because of the plasma wall contact. Then, I will give an overview of an electronegative especially reactive

plasma for instance an oxygen plasma as used in the experiment.

Here, the plasma wall interaction and secondary particle emission will be of interest. I will show possible production processes and describe the resulting particle fluxes.

To get the microscopic information it is suitable to apply plasma simulations based on kinetic models. In this thesis I will use a Particle-In-Cell (PIC) method with Monte-Carlo-Collisions (MCC) [5]. Improving the numerical performance is needed to be able to simulate realistic scenarios in reasonable run-times. Therefore, the concept of parallelization will be introduced and its advantages and limits will be discussed.

As a first step for the analysis, I will make use of a one-dimensional model to simulate the center of the discharge without asymmetry effects. Later, I want to transfer the results on a two-dimensional model where the asymmetric behavior is treated self-consistently.

My goal is to simulate an electronegative plasma with additional surface effects, which allows us an interpretation of the experimental results as seen in figure (1.1).

2 Basic principles of plasma physics

Before I start my simulation I need to take a closer look on some basic plasma properties. I will focus on rf plasmas and plasma wall interaction because of the importance of the walls as an ion source. For detailed insight on nonthermal plasma chemistry and physics I refer to [3].

A plasma is an ionized gas, showing collective behavior. In general it consists of electrons, neutrals and ions of different charge. These species are denoted by the index s. The quasi-neutral region of a plasma is called bulk. In the bulk the densities of charged particles are equal. Due to the mobility of the electrons, the plasma shields electric fields. The understanding of the interaction between a plasma with walls is particularly important for the application of rf plasmas, therefore I introduce this topic here.

2.1 Plasma wall interaction

Next to a wall the quasi-neutrality of the plasma vanishes and charge separation builds up a negative potential drop. This happens because the electrons are much faster than the ions, due to their lower mass. The potential drop influences the particle densities and the energy distributions. This region is called plasma sheath. It is usually of the size of a few Debye-length

$$\lambda_{Db} = \sqrt{\frac{\varepsilon_0 k_B T_e}{n_e e^2}} \, , \tag{2.1}$$

(with the Boltzmann constant k_B, the electron temperature T_e the electron density n_e and elemental charge e), which is the shielding length of a plasma.

The sheath characteristics are mostly influenced by the physics of the wall. Here, we will shortly discuss the idea of an ideal absorbing wall, secondary electron emission and an ion emitting wall.

The simplest model is an ideal absorbing wall, which only considers recombination at the wall. While the velocity of the electrons is much higher, more electrons than ions impinge on the wall. This results in a negative potential drop which accelerates the ions. Over time both specie densities decrease. At steady state both fluxes for electrons Γ_e and ions Γ_i at the wall must be equal

$$\Gamma_e = \Gamma_i \, . \tag{2.2}$$

The potential drop from the plasma potential to the wall $\Delta\Phi$ leads to the reflection of electrons with a lower energy than $e\Delta\Phi$. The ions accelerate in the sheath and the electrons

get reflected. This leads to a decreasing electron density at the wall (see figure 2.1). The resulting electron current density at the wall is then given by

$$j_e = -\frac{e}{4} n_e \langle v \rangle \exp\left(\frac{-e\Delta\Phi}{k_B T_e}\right) \; , \qquad (2.3)$$

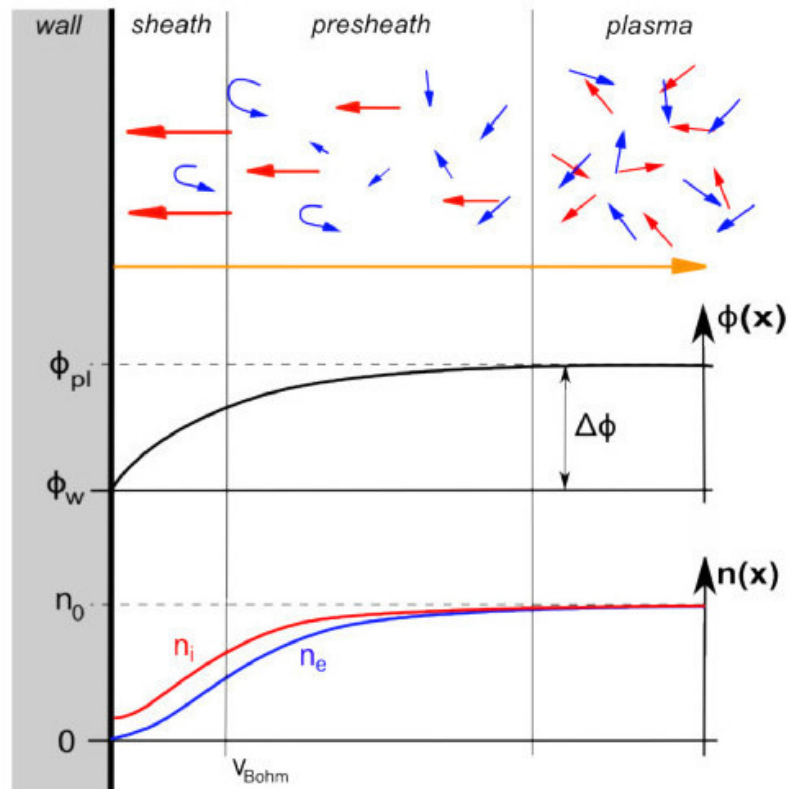with the first moment of the electron velocity $\langle v \rangle$.

Figure 2.1: Sketch of the important processes in a plasma sheath, taken from [6]. Red arrows represent ions, blue arrows represent electrons and orange represents reflected neutrals. At the bottom the resulting potential and particle densities are shown.

The impinging ions are neutralized by wall electrons near the wall. The resulting neutrals are reflected at the wall in this simple model and much later get ionized again. But the mean free path is usually longer than the sheath so in many cases we can consider the sheath collisionless.

For zero net current $(j_e = j_i)$ at the wall the drop between plasma potential and the wall can be estimated as

$$e\Delta\Phi \approx -k_B T_e \ln\left(\sqrt{\frac{m_i}{2\pi m_e}}\right) \; . \qquad (2.4)$$

If impinging electrons lead to the emission of electrons from the wall one talks about secondary electron emission. The additional negatively charged particles from the wall lead to a smaller potential drop. This is due to less electrons from the bulk need to be reflected to obtain steady state condition, which means the current is equal to zero. Considering the reduced incoming electron flux we receive an effective potential drop

$$e\Delta\Phi^{eff} = -k_B T_e \ln\left((1-\gamma)\sqrt{\frac{m_i}{2\pi m_e}}\right) \, , \tag{2.5}$$

with the emission coefficient γ describing the ratio of secondary electron flux to primary electron flux. In a previous thesis it is shown that for higher values than a critical value γ_c the wall potential becomes unstable [6]. In my upcoming simulation we will always operate in save regimes with respect to the secondary electron emission coefficient ($\gamma = 0.01$).

2.2 Surface effects and secondary ion emission

In comparison to the secondary electron emission there also exists **s**econdary **i**on **e**mission (SIE). This process is of particular interest for this work, because the experimental results of the velocity distribution of negative ions measured at the grounded electrode indicate surface production of negative ions. Theoretical studies of surface ionization are mostly devoted to the production of positive ions from incident atoms having thermal energies [7]. When an atom M impinges on a positively biased metal surface at a high temperature the valence level is broadened. For a mean residence time τ electrons can move between the metal and the atom when the valence level is sufficiently broadened. Thus, a positive ion or an atom is emitted after the equilibrium

$$M \rightleftharpoons M^+ + e^- \text{ (in the substrate metal)} \tag{2.6}$$
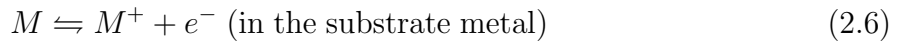
is attained at the surface (thermal ionization). This process is of statistical nature. Hence, the degree of ionization can be derived by applying thermodynamic arguments. The probability of ionization mainly depends on the substrate temperature T, the work function of the substrate and the ionization energy of the atom. A detailed derivation can be found in [8]. The ionization coefficient of M is then given by

$$\begin{aligned} \alpha^+(M^+) &= \frac{n^+}{n} \\ &= \frac{1-r^+}{1-r} \cdot \frac{w^+}{w} \exp\left(\frac{\bar{\Phi}^+ + e\sqrt{eF} - I(M)}{k_B T}\right) \, , \end{aligned} \tag{2.7}$$

where n^+ and n are the numbers of M^+ and M coming from unit surface area per unit time, w^+/w is the statistical weight ratio of M^+ to M, r^+ and r are the internal reflection coefficients at the potential barrier on the emitter surface, $\bar{\Phi}^+$ is the average work function, T is the absolute temperature at the surface, F is the externally applied field and $I(M)$ is the initial energy of the impinging atoms.

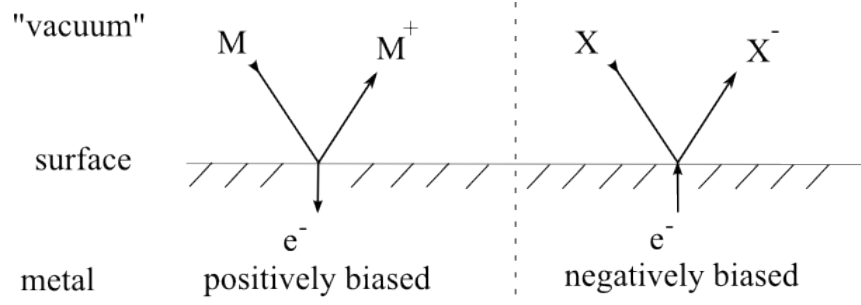The basic interaction of an incoming atom with the wall is shown in figure (2.2). For

Figure 2.2: Schematic interaction of an atom beam with a positively or negatively biased metal substrate.

positive ions and for high temperatures ($\geq 1000\,$K) this coefficient is discussed by several authors, e.g. [9]. For high temperatures the reflection coefficients r^+ and r are considered to be zero. Additionally the Schottky term $e(eF)^{1/2}$ is less than $0.012\,$eV for $F < 1\,$kV and can be neglected too. To my knowledge there is no accurate study of these coefficients for low temperatures of about 300 K.

With little adaptations I can transfer equation (2.7) for treating a surface which emits negative ions. I assume a negatively biased surface like the cathode in an asymmetric ccrf discharge where the equilibrium

$$X + e^- \text{ (in the substrate metal)} \leftrightharpoons X^- \tag{2.8}$$
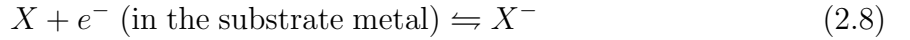
is attained at the surface. Hence, the equation for the negative ionization coefficient follows in analogy to equation (2.7)

$$\begin{aligned}
\alpha^-(X^-) &= \frac{n^-}{n} \\
&= \frac{1-r^-}{1-r} \cdot \frac{w^-}{w} \exp\left(\frac{-\bar{\Phi}^- + e\sqrt{eF} + A(X)}{k_B T} \right) ,
\end{aligned} \tag{2.9}$$

where $A(X)$ is the electron affinity of atom X, $\bar{\Phi}^-$ is the average work function effective for producing the negative ion X^- on the metal surface and the other parameter are in analogy to the positive ion injection. If one assumes high temperatures (reflection coefficients are equal to zero), neglect the Schottky term and assume a homogeneous substrate in respect to the work function (namely $\bar{\Phi}^- = \bar{\Phi}^+ = \Phi$) one receives the Saha-Langmuir equations

$$\alpha^+(M^+) = \frac{w^+}{w} \exp\left(\frac{\bar{\Phi}^+ - I(M)}{k_B T} \right) , \tag{2.10}$$

$$\alpha^-(X^-) = \frac{w^-}{w} \exp\left(\frac{A(X) - \bar{\Phi}^-}{k_B T} \right) . \tag{2.11}$$

These equations apply to an atomic-beam surface interaction. Similar equations can be derived for a molecular-beam surface interaction [7]. For ccrf discharges the approximations taken for equation (2.10) cannot be applied due to the fact that one has a homogeneous metal substrate and the work function is therefore equal in the positive and negative case. To the best of my knowledge. there are no detailed theoretical and experimental studies

of the reflection coefficients r for negative ions.

One of the few works on negative ion production was done by Ustaze et al [10]. They studied electron capture and loss processes during the scattering of atoms and anions on a MgO(100) surface. There they discussed negative ions produced by electron transfer processes at a wall, determined by ion beam scattering studies, which has been amply demonstrated for metal surfaces, for example in [11]. For oxide surfaces there are few studies yet. Ustaze et al studied the interaction of oxygen atoms and anions with magnesium oxide (MgO). The results showed that impinging atoms at the MgO surface created also anions. The idea for such a process is that an oxygen atom O captures an electron from the surface and becomes a negative ion O^-. This interaction is strongly energy dependent with higher capture rates at low energies ($<1\,\text{eV}$). The electron capture can be treated as a non-resonant charge transfer process at the oxygen anion site. This happens because of the strong charge locality in magnesium oxide. In a MgO crystal one considers Mg^{++} and O^{--}. If an atom O gets close to the surface it may capture one electron of the anion of MgO.

In addition, electron losses can appear. So for a complete description both reactions have to be taken into account. A good overview of methods for the production of negative ions in general is given by H. Kawano [7].

Still the theoretical background for surface ion production is missing. Therefore no detailed information about the cross-sections for such processes exists. In this work I assume that negative ions are produced by a positive ion beam on the surface with an efficiency of $\eta = n_-/n_+$.

The additional flux of negatively charged particles leads to a reduction of the potential drop as in the case of secondary electron emission. As for the electrons the injection coefficient η determines the ratio of injected ions. The same stability criteria as for the secondary electron emission coefficient γ apply. If one chooses η greater than a critical value η_c the plasma gets unstable because of the high ion flux from the wall and a double sheath could develop.

The injected negative ions from the surface will be accelerated by the potential drop towards the plasma where they can reach high energies and this is considered as a possible reason for the high-energy peak in the measured distribution of negative oxygen ions in the ccrf discharge.

2.3 Capacitively coupled radio frequency (ccrf) plasma

I am interested in ccrf plasmas, which are driven by an radio frequency ($\omega_{rf} = 13.56\,\text{MHz}$). The basics of rf discharges are treated in [3] and here I just want to discuss the most important aspects for this thesis. The rf leads to time dependent plasma conditions within the rf cycles, because the distribution functions, potential and all macroscopic quantities, like densities and velocities, are time dependent. The ccrf discharges are characterized by the condition

$$\omega_{p+} < \omega_{rf} < \omega_{pe} \,, \tag{2.12}$$

where ω_{p+} and ω_{pe} are the respective plasma frequencies of positive ions and electrons [3].

Due to the rf frequency the potential at the cathode changes over time. The ions react slowly to the changing field. Due to their much higher mass they have a much smaller mobility than the electrons. Hence, they move on a timescale larger than one rf cycle. But the electrons can follow the fields rapid changes. This leads to a shift in the electron density depending on the phase of the rf which is equal to an oscillating sheath. In figure (2.3) the sheath dynamic is shown.
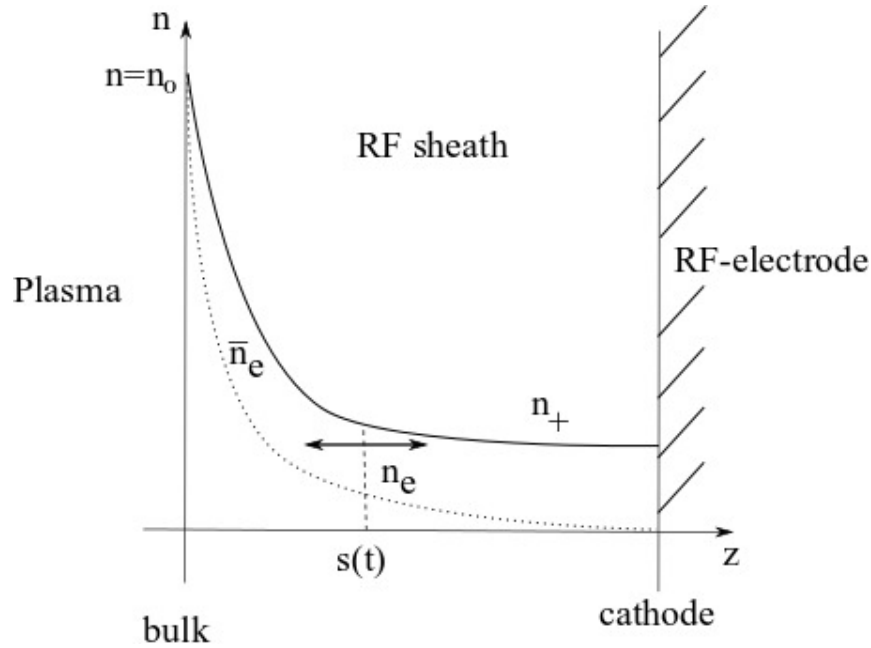

Figure 2.3: Rf sheath with density profiles and moving electron sheath edge

2.3.1 Strongly asymmetric ccrf discharges

Most unconfined rf plasmas are asymmetric due to their wall contact. When talking about asymmetry I refer to the area ratio of the powered cathode A_{rf} to the grounded anode and the wall of the plasma chamber $A_{grounded}$. When the rf power is applied the fast electrons impinge the electrodes. Since there cannot be a net current over one rf cycle a negative voltage at the cathode builds up. This is the self-bias voltage.

The negative potential shift at the cathode leads to a higher ion flux towards the cathode until the ion flux is the same as the electron flux $\Gamma_i = \Gamma_e$.
In ccrf discharges the self-bias voltage is a little less than half the peak-to-peak voltage $|\varphi_{sb}| \approx \frac{1}{2}\varphi_{pp} = \varphi_0$. This leads to a voltage φ_{rf} of

$$\varphi_{rf} = -\varphi_{sb} + \varphi_0 \sin(\omega_{rf}t) \tag{2.13}$$

at the powered cathode. The rf power primarily influences the sheath dynamics and the self-bias voltage. One industrial application of a ccrf plasma is plasma etching. It uses the self-bias voltage to produce fast ions which impinge the substrate at the cathode [1].
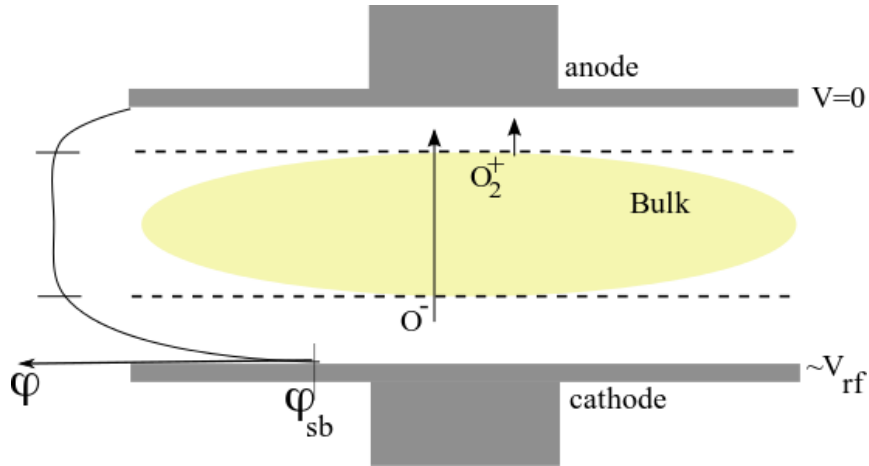
Figure 2.4: Processes in the plasma chamber. The rf-driven cathode is at the bottom and the grounded anode at the top.

2.3.2 Electronegative plasmas

In comparison to standard plasmas (i.e. argon or xenon) which consist of electrons, positive ions and neutrals, a electronegative plasma also contains negative ions. The degree of electronegativity α is given by the ratio of negative ions to electrons in the bulk

$$\alpha = \frac{n_-}{n_e} \ .$$
(2.14)

Electronegative plasmas are characterized by $\alpha > 1$.

They are of high importance for plasma-assisted material processing [2]. The main volume production channel of negative ions formed in low pressure plasmas is the dissociative attachment of an electron to a molecule

$$e^- + \mathrm{AB} \to \mathrm{A} + \mathrm{B}^- \ .$$
(2.15)

When an electron attaches to a neutral molecule it gets excited. Because the time scale of an electronic excitation is very short ($< 10^{-15}$ s) the molecule distance does not change when excited, as used in the Born-Oppenheimer approximation. The molecule is then excited to a real or virtual state, which has a curve crossing with a dissociative state (s. figure 2.5). The fragments can be produced with significant kinetic energy.

Another channel for negative ion production is through three-body non-dissociative attachment. In the following I focus on the ions produced by the dissociative attachment because their production rate is several magnitudes larger in the considered system due to the low pressure so that three-body processes can be neglected.

Negative ions can get lost through multiple reactions. In my later model I will consider neutral detachment, impact detachment and neutralization
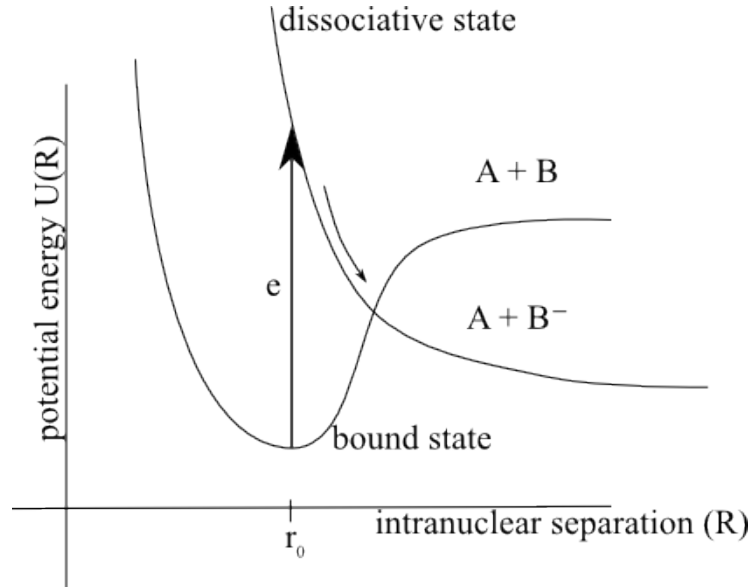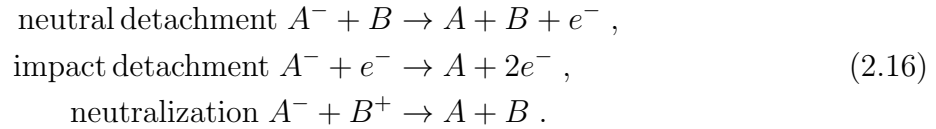
Figure 2.5: Schematic process of dissociative attachment. An electron attaches to the
molecule AB which then dissociates into a neutral atom A and a negative
ion B^-.

$$\begin{aligned}
\text{neutral detachment } & A^- + B \to A + B + e^- , \\
\text{impact detachment } & A^- + e^- \to A + 2e^- , \\
\text{neutralization } & A^- + B^+ \to A + B .
\end{aligned} \qquad (2.16)$$

The corresponding cross sections can be found in chapter 2.4.1.
Similar to positive ions charge exchange collisions are also calculated with the negative ions

$$\text{charge exchange } A + B^- \to A^- + B , \qquad (2.17)$$
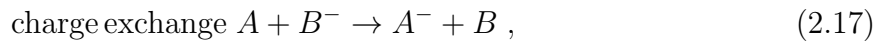
which becomes important when surface effects are introduced. The fast ions coming from
the surface will cool down through charge exchange collisions and hot neutrals are pro-
duced.
In principle, negative ions behave like heavy, cold electrons ($T_i << T_e$). They obey the
same kinetic and transport laws. For conventional low pressure plasmas negative ions are
confined by the plasma potential. The main loss channel is hence by volumetric processes.
This leads to a density distribution (s. figure (2.6)) with an electronegative core and re-
gions where negative ions are excluded [12].

One kind of electronegative plasmas is an oxygen plasma which plays an important role
for etching and thin-film deposition techniques [1].
The existence of negative ions has a huge impact on the plasma characteristics, as it
changes the ion density distribution which leads to a central quasi-neutral ion-ion plasma
and a peripheral electron-ion plasma. The electronegativity α leads to different kinds of
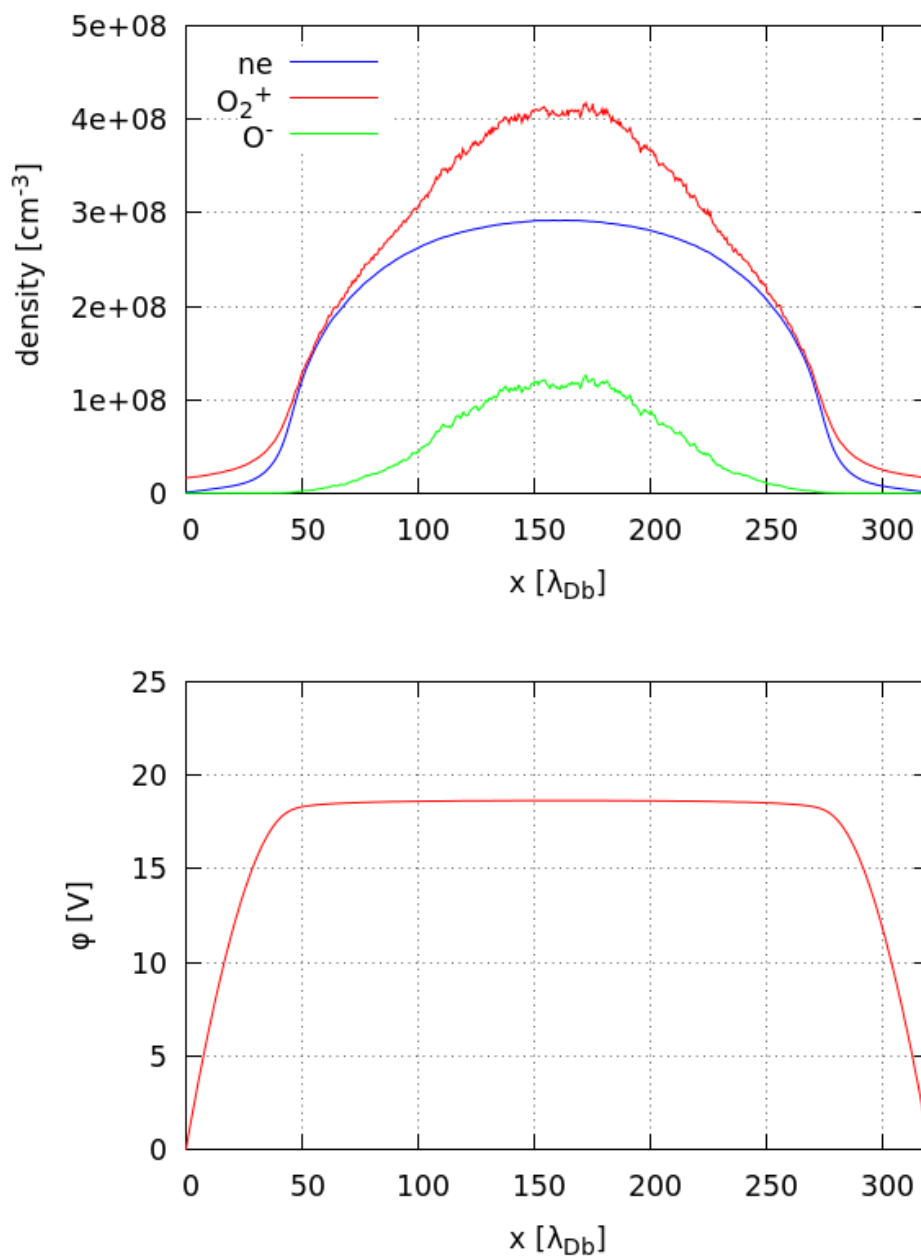
Figure 2.6: Example of a 1D PIC simulation of oxygen plasma showing plasma potential and density distributions averaged over many rf cycles.

instabilities. At this point I only mention the attachment-induced ionization instability in oxygen plasmas [13]. A small initial increase of the electron density leads to a shift of the equilibrium state between ionization and electron attachment processes. Under special conditions an additional increase of the electron density via a decrease in electron temperature is possible. The plasma becomes unstable and electron density fluctuations take place. These fluctuations are equivalent to fluctuations of the negative ion density because of the strong coupling between the electron density and the attachment process. But this instability is only to happen at high pressures (>30 Pa) and for certain rf powers.

Now, most important physics elements needed for this work are covered. For more details I refer to the standard literature, e.g. [3].

To get a microscopic knowledge of a ccrf discharge the discharge is simulated. Since nonthermal low pressure plasmas are not collision dominated the particles are not Maxwell distributed. The mean free paths are of the same magnitude as the electrode gap. This means that fluid models fail at this point and kinetic models have to be applied. I will use the PIC-MCC method which is widely used for plasma simulation. In the next chapter I will give details about the implemented PIC method.

2.4 PIC-MCC

Particle-**i**n-**C**ell with **M**onte-**C**arlo-**C**ollision (PIC-MCC) methods simulate the motion of each particle (e.g. in a plasma) in continuous phase space while macro-quantities like densities or potentials are computed on stationary mesh points. In plasma physics applications, the method follows the trajectories of charged particles in self-consistent electromagnetic (or electrostatic) fields computed on a fixed mesh. The macro-force is then calculated from the field equations. Macro forces are used because otherwise one would have to consider particle-particle interaction which scales quadratically with the particle number N^2. The particle mesh method just scales with $N \log N$ and is hence much faster for a big particle number [5].

2.4.1 Basics of a PIC simulation

I will refer only to the electrostatic case since no magnetic field is applied and one can neglect magnetic fields from moving charged particles, because their resulting forces are very small compared to the electric forces produced by the charge densities and applied voltage.

The plasma species s is described by the distribution function $f_s(\vec{x}, \vec{v}, t)$. The evolution of the distribution f_s is given by the total time derivative, resulting the Boltzmann equation

$$\frac{\partial f_s}{\partial t} + \vec{v} \cdot \nabla_{\vec{x}} f_s + \frac{Z_s e}{m_s} \vec{E} \cdot \nabla_{\vec{v}} f_s = \left(\frac{\partial f_s}{\partial t} \right)_{coll} , \qquad (2.18)$$

with the electrostatic force $\frac{Z_s e}{m_s}\vec{E}$ acting on the particle and $\nabla_{\vec{x}}$ and $\nabla_{\vec{v}}$ denoting the space and velocity gradient respectively. The right hand side $\left(\frac{\partial f_s}{\partial t}\right)_{coll}$ considers the time dependent change of f_s due to to collisions.

The moments of the distribution function f_s yield the macroscopic plasma properties. The 0th moment describes the species s charge density

$$n_s(\vec{x}, t) = q_s \int f_s(\vec{x}, \vec{v}, t)\mathrm{d}\vec{v} \; , \tag{2.19}$$

and the first moment in velocity space gives the mean velocity of s

$$u_s(\vec{x}, t) = \frac{1}{n(\vec{x}, t)} \int \vec{v} f_s(\vec{x}, \vec{v}, t)\mathrm{d}\vec{v} \; . \tag{2.20}$$

So one can rewrite the distribution function as

$$f_s(\vec{x}, \vec{v}, t) = \frac{n_s(\vec{x}, t)}{q_s} \hat{f}_s(\vec{x}, \vec{v}, t) \; , \tag{2.21}$$

with the normalized velocity distribution $\hat{f}_s$. In thermodynamical equilibrium this distribution takes the form of the Maxwell-Boltzmann-equation

$$f_s^m(\vec{x}, \vec{v}, t) = \frac{n_s(\vec{x}, t)}{q_s} \left(\frac{m_s}{2\pi k_B T_s}\right)^{3/2} \exp\left(-\frac{|\vec{v}|^2}{v_{th,s}^2}\right) \; , \tag{2.22}$$

with the species temperature T_s and the thermal velocity $v_{th,s} = \sqrt{\frac{2k_B T_s}{m_s}}$.

Instead of kinetic simulations there is also the possibility to approximate a plasma as a charge carrying fluid. The resulting fluid equation is acquired by multiplying the particle motion of species s with its density n_s

$$m_s n_s \frac{\mathrm{d}\vec{u}_s}{\mathrm{d}t} = q_s n_s \vec{E} \; , \tag{2.23}$$

and applying the convective derivative

$$\frac{\mathrm{d}\vec{u}_s}{\mathrm{d}t} = \frac{\partial \vec{u}_s}{\partial t} + (\vec{u}_s \cdot \nabla_{\vec{c}})\vec{u}_s \; , \tag{2.24}$$

to observe the fluid elements in a fixed spatial frame. Still the thermal motion has to be taken into account which generates a pressure force $-\nabla_{\vec{x}}\mathbf{P}$. If the species s is Maxwell distributed the stress tensor will reduce to the scalar pressure p=$\frac{n_s k_B T_s}{V}$. In this case the calculation expense of fluid approximations is drastically lower than for kinetic particle tracking simulations.

The stress tensor $\mathbf{P}$ gets very complex when the species s is not Maxwell distributed. In collision-dominated plasmas, which means that the mean free path is small, the Maxwell distribution is a very good approximation and fluid models are adequate. But in low temperature plasmas, especially in the sheath, the mean free paths are long and Maxwell distribution is not guaranteed.

Using the PIC method one solves the equation of motion of N particles

$$\frac{\mathrm{d}\vec{x}_i}{\mathrm{d}t} = \vec{v}_i \tag{2.25}$$

$$\frac{\mathrm{d}\vec{v}_i}{\mathrm{d}t} = \vec{F}_i\left(t, \vec{x}_i, \vec{v}_i, \vec{E}\right) \tag{2.26}$$

and the electric field $\vec{E}$ self-consistently. The force acting in a plasma is the Lorentz-force F_L (I just consider the non-relativistic electrostatic case for simplicity)

$$\frac{d\vec{v}_i}{dt} = \frac{q_i}{m_i}\vec{E}(\vec{x}_i) \tag{2.27}$$

for i=1,...,N. The electric field has to be calculated from the particle position $\vec{E} = \vec{E}(\vec{x}_1, ..., \vec{x}_N)$ using the Poisson equation for an electrostatic potential $\Phi(\vec{x}, t)$ and the resulting electric field $\vec{E}(\vec{x}, t)$:

$$\Delta\Phi(\vec{x}, t) = -\rho(\vec{r}, t)/\varepsilon_0 \,, \tag{2.28}$$
$$\vec{E}(\vec{x}, t) = -\nabla\Phi(\vec{x}, t) \,, \tag{2.29}$$

and an interpolation is schemed for the charge density ρ

$$\rho = \rho(\vec{x}_i, \vec{v}_1, ..., \vec{x}_N, \vec{v}_N) \ . \tag{2.30}$$

One timestep of a PIC model contains different parts as shown in figure (2.7).
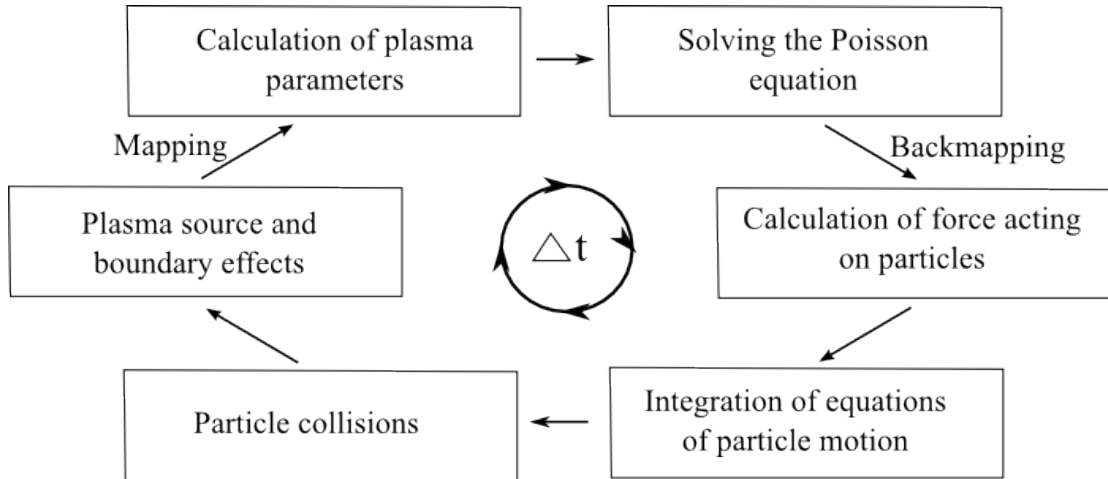
Figure 2.7: Scheme of the PIC simulation

For more information about PIC simulation models I refer to standard literature, especially [5]. Here I just shortly outline the main parts of a PIC cycle.

Domain composition

Before the PIC simulation starts the domain, on which the discharge is simulated, has to be defined. A 1d3v and a 2d3v-PIC simulation in a cylindrical coordinate system are calculated where the space will be resolved in one and two dimensions (r and z) and the velocity in three dimensions (v_r, v_z, v_ϑ) respectively. The spatial resolution has to be less than the smallest length scale, in my case usually the Debye length λ_{Db}. The time resolution has to be less than the fastest process, usually the electron plasma oscillation ω_{pe}

$$\omega_{p,e} = \sqrt{\frac{n_e e^2}{\varepsilon_0 m_e}} \ . \tag{2.31}$$

So the distance Δx_i between two grid points of the used mesh equals half a Debye length $\lambda_{Db}/2$ and the resolved time Δt equals one fifth of the plasma frequency $\omega_{pe}/5$. These conditions

$$\Delta x = 0.5 \lambda_{Db} \ , \tag{2.32}$$

$$\Delta t = \frac{0.2}{\omega_{pe}} \ , \tag{2.33}$$

satisfy the stability criteria (s. chapter 2.37).

The time-step and the size of our domain are defined by the electron temperature T_e and electron density n_e. The initial electron Temperature $T_e = 4\,\mathrm{eV}$ and the electron density $n_e = 5 \cdot 10^9\,\mathrm{cm}^{-3}$ are set. The resulting Debye length is $\lambda_{Db} = 0.02101\,\mathrm{cm}$.

The algorithm has a dimensionless form where all properties are set in relation to the Debye length and the plasma frequency. After the simulation one has to check the results to see that the correct densities and temperature are used. If not chosen correctly over- or worse underresolution will occur. An overresolution will take up more computation time than necessary and an underresolution might lead to unphysical behavior. The number of cells have to be chosen to cover the experimental domain. For most of the simulations the number of cells in one dimension is set to 640. This results in a 1d3v discharge with a gap between the electrodes of $6.72\,\mathrm{cm}$.

Plasma source

To start the simulation one has to ignite the discharge. This means one has to initialize the particles accordingly. In a real system the number of particles is very high (usually $> 10^{12}$). Moving every one of them would take up too much computational time. One can make use of the fact that the Lorentz-force F_L (equ. (2.29)) just depends on the charge to mass ratio and introduce super particles. Every one of these super particles represents thousands of real particles and follows the same trajectory. With an electron density of $10^8 - 10^9\,\mathrm{cm}^{-3}$ and an electron temperature of $4\,\mathrm{V}$ one simulated particle represents ≈ 6000 real particles in my simulation.

It was shown that the introduction of super particles does not introduce any artefacts and guarantees the exact solution [14], if the weight is not too high.

To initialize the particles I put an equal amount of Maxwell distributed neutrals, electrons and positive ions equally distributed into the domain. This is done to save computation time. In addition the phase of plasma and sheath formation is very fast. The plasma will relax into a steady state after a certain amount of time. After the first initialization the only particle sources are from collisions, secondary electron emission and secondary ion emission (chapter 2.1) and the plasma is self consistent. The relaxation takes up hundreds of rf cycles. Accordingly, the calculation time needs to cover this time.

Potential calculation

Now the domain is filled with particles and the resulting potential has to be calculated. Numerical solvers need a discrete distribution function. Hence, one has to map the charged particles onto a discrete mesh with a spatial resolution of $\lambda_{Db}/2$ covering the domain. The charge densities needed for the Poisson equation are calculated by applying a linear weighting scheme of first order as illustrated in figure (2.8), which gives the particles a shape. This is called the Cloud-in-Cell (CIC) weighting scheme.
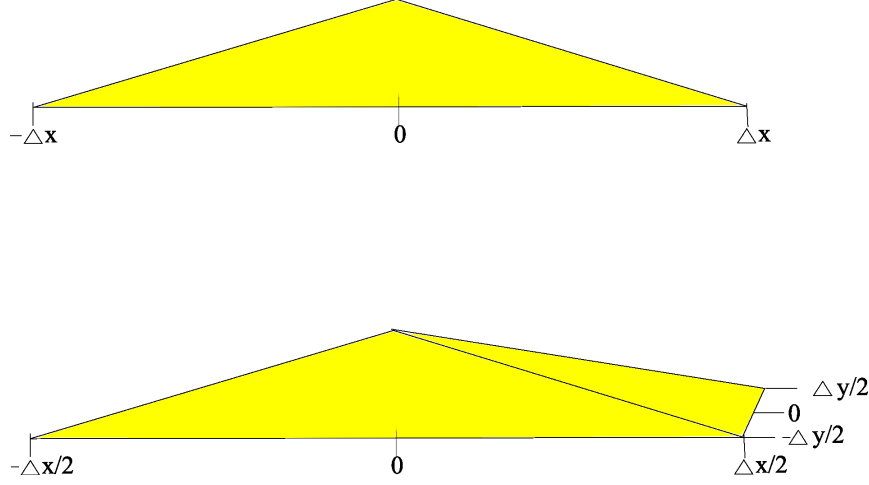
Figure 2.8: CIC weighting scheme in one and two dimensions.

Assuming the finite difference two-dimensional mesh with the grid points located at (x_i, y_i) the weight of the particle is given by

$$n_{i,j} = \frac{S_{i,j}}{A_{i,j}^2}(x_{i+1} - x)(y_{i+1} - y),$$

$$n_{i+1,j} = \frac{S_{i+1,j}}{A_{i+1,j}^2}(x - x_i)(y_{i+1} - y),$$

$$n_{i,j+1} = \frac{S_{i,j+1}}{A_{i,j+1}^2}(x_{i+1} - x)(y - y_i) \text{ and}$$

$$n_{i+1,j+1} = \frac{S_{i+1,j+1}}{A_{i+1,j+1}^2}(x - x_i)(y - y_i) \,, \tag{2.34}$$

with $n_{i,j}$ is the density, (x_i, y_i), $S_{i,j}$ the statistical weight and $A_{i,j} = \Delta x \Delta y$, each one at the grid point (x_i, y_i). The one-dimensional weighting follows analogously. Using the same weighting scheme one can also calculate other macro properties on the mesh, like number densities. The weighting scheme becomes important again when one calculates the force acting on the particles (see chapter 2.29). To ensure that the force acting on the particles is physically correct (e.g. avoiding possible self-forces) one has to make sure that the weighting is consistent as well. Of high importance is the conservation of momentum which is achieved by choosing the same weighting function when calculating the force.
To solve for the potential boundary conditions have to be applied. So the rf-potential

at the cathode is set and the anode is grounded. The Poisson equation for the charge distribution $\rho(n_e, n_i)$

$$\Delta\Phi(\vec{r}) = \frac{\rho(n_e, n_i)}{\varepsilon_0} \tag{2.35}$$

becomes a matrix equation when discretized. This matrix equation gets inverted by a LU-factorization [15] on the given mesh and the potential is calculated in every time step by back solving the solution with the current charge distribution. The LU-factorization has to be done only one time at the start of the simulation, because the discretization matrix of the left side depends only on the mesh metrics, which does not change during the PIC run.

Force calculation

The obtained potential is a discrete one, defined only on the grid points. To calculate the force from equation (2.29) onto the particle positions which are distributed continuous over the domain and not just at the grid points one has to calculate the force F_i by applying the same weighting scheme as before (see figure 2.8). This and the fact that the applied mesh has a constant grid size, will conserve the particle momentum which in turn avoids artefacts like self-forces for equidistant meshes.

Particle mover

With the force acting on the particles they are pushed accordingly. For that the equations of motion (equ. (2.27)) are solved and the particles are moved. For solving these equations the Boris algorithm is used, which is most suited for this case. It is a leap-frog algorithm. The Boris pusher serves speed and long time accuracy. It is applied by the equations

$$\boldsymbol{x}_{k+1} = \boldsymbol{x}_k + \Delta t \boldsymbol{v}_{k+1/2}, \tag{2.36}$$
$$\boldsymbol{v}_{k+1/2} = \boldsymbol{u}' + q' \boldsymbol{E}_k, \tag{2.37}$$

with

$$\begin{aligned} \boldsymbol{u}' &= \boldsymbol{u} + \boldsymbol{u} * \boldsymbol{s} \ , \\ \boldsymbol{u} &= \boldsymbol{v}_{k-1/2} + q' \boldsymbol{E}_k \ , \\ q' &= \Delta t * (q/2m_s). \end{aligned} \tag{2.38}$$

For more information about the Boris algorithm I refer at this point to the standard literature [16]. For my purpose I just push the charged species. It is not necessary to calculate the motions of the neutrals because they are just considered as a homogeneous background. This is an acceptable approach because the mean free path of my neutral particles is about

$$\begin{aligned} l_{mfp} &= \frac{k_B T}{\sigma p} \\ &= \frac{k_B \cdot 300\,\mathrm{K}}{\sigma \cdot 10\,\mathrm{Pa}} \approx 4\,\mathrm{cm} \ , \end{aligned} \tag{2.39}$$

where σ is the cross section of the collision of plasma particles with neutrals. For even lower pressures the mean free paths are of the dimension of my discharge (namely the electrode gap).

Subcycling

The particle mover is applied to electrons in each time-step but it is not necessary to move the ions that often. Because of their much lower velocity they act on a different time scale. To save calculation time they are pushed every few steps only. One has to sum up and average the force acting on them in the meantime. The subcycling factor must also be applied in the collision routine. Because the particle mover and the collisions are the most time consuming parts, the subcycling of the ions saves a lot of calculation time.

Boundary conditions

Because of a bounded plasma the plasma wall interaction is not trivial. When a primary particle (electron, ion, neutral) is absorbed by a wall it can cause the emission of a secondary particle (including simple reflection). To solve this issue Monte-Carlo methods are used. A random number R between 0 and 1 is compared with the general emission probability $F(\epsilon, \alpha)$ depending on the particle energy ϵ and the incidence angle α. If F>R then a secondary particle is injected with a velocity given by a predefined distribution $f_{sec}(\vec{v})$. Otherwise the particle is lost.
I use this to realize secondary electron emission and secondary ion emission.

Collisions

If the particles only move according to macro fields the simulated plasma is collisionless. In order to simulate a collisional plasma, collision routines have to be implemented. One could calculate every particle-particle interaction which scales with N^2. A better solution for the Coulomb collisions is the binary collision model [5] . In this model only particles in a Debye-cell collide, while self-forces are avoided. This is of sufficient accuracy.
For charged particle collisions a null collision method is used. The particle flux changes due to collisions in the volume from x to x + dx

$$\frac{\mathrm{d}\Gamma}{\mathrm{d}x} = -n_s\sigma\Gamma \; , \tag{2.40}$$

which results in total flux of

$$\Gamma(x) = \Gamma(0)\exp\left(-\frac{x}{n_s\sigma}\right) \; , \tag{2.41}$$

where the factor $1/(n_s\sigma) = \nu t = \lambda_{mfp}$ equals the mean free path. This leads to the collision probability

$$P(t) = 1 - \exp(-\nu t) \; , \tag{2.42}$$

which is the basis for the Monte Carlo method. A charged particle is picked and it is collided with a randomly picked neutral particle of the same Debye-cell if the collision probability

Table 2.1: Collisions and reactions included in the simulation

Electron energy loss scattering

(1)	e + O_2	$\rightarrow$ e + O_2 (ν= 1, ...,4)	Vibrational excitation
(2)	e + O_2	$\rightarrow$ e + O_2 (Ryd)	Rydberg excitation
(3)	e + O_2	$\rightarrow$ e + $O(3P)$ + $O(3P)$	Dissociation (6.4 eV)
(4)	e + O_2	$\rightarrow$ e + $O(3P)$ + $O(1D)$	Dissociation (8.6 eV)
(5)	e + O_2	$\rightarrow$ e + $O_2(a^1\Delta_g)$	Meta-stable excitation
(6)	e + O_2	$\rightarrow$ e + $O_2(b^1\Sigma_g)$	Meta-stable excitation

Electron and ion production and loss

(7)	e + O_2^+	$\rightarrow O + O$	Dissociative recombination
(8)	$O^- + O_2^+$	$\rightarrow O + O_2$	Neutralization
(9)	e + O_2	$\rightarrow O + O^-$	Dissociative attachment
(10)	$O^- + O_2$	$\rightarrow O + O_2$ + e	Direct attachment
(11)	e + O_2	$\rightarrow$ 2e + O_2^+	Electron impact ionization
(12)	e + O^-	$\rightarrow O$ + 2e	Electron impact detachment

P at time t is bigger than a random number between 0 and 1. Here $\nu = \sum_{i=1}^{I} \nu_i$ is the sum of all possible collision frequencies. ν depends on plasma parameters

$$\nu_i = \sigma_i(V)n_i \,, \tag{2.43}$$

where σ_i is the collision cross-section, V is the relative velocity and n_i the target particles density. The cross-sections of the implemented collisions are given in chapter (2.4.1). For more detailed information of the used MCC (Monte-Carlo-Collisions) methods I refer to [5].

Collisions in oxygen

The plasma chemistry of oxygen is quite complicated and there are over 75 reactions known that may occur. In my model I just include the most important collisions. In advance the selection of these collision has been done already [17].
As discussed before, the most interesting collision in this specific case studied here is the dissociative attachment (table (2.1) collision (9)) because it is the primary volume source of negative ions (see also chapter (2.3.2)). I will later analyse where the negative ions and how their energy distribution are formed. In addition to the shown collisions, elastic/coulomb scattering and charge exchange collisions (O_2, O_2^+) and (O^-, O_2) are included.

The respective cross-sections are shown in figure (2.9). Compared with the other cross sections the one of the associative detachment is of one to two orders of magnitude smaller. The cross-section for dissociative attachment is given for energies between $3 - 15$ eV. If two particles with an energy lower than that collide the cross-section of 3 eV is taken, due to missing data. Respectively, it is the same for higher energies > 15 eV.
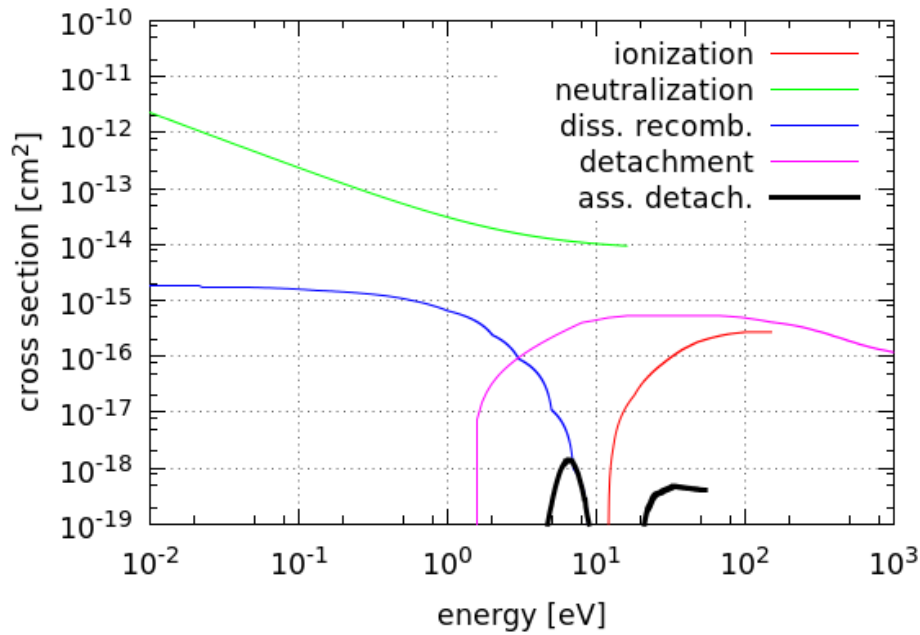
Figure 2.9: Cross-section of the dissociative attachment $O_2 + e^- \rightarrow O^- + O$ as a function of energy.

Another source of charged particles is the ion emission at the wall. An injection of a negative ion is implemented when a positive ion hits the wall. The ratio of the number of impinging ions and the number of emitted negative ions is further named as η. As discussed before, no cross sections exist and this coefficient is used as a fit parameter to get closer to the experimental observations. I will see that I can simulate a plasma which energy distribution functions are close to experimental results by injecting negative ions at the powered cathode.
Future studies will have to show what processes lead to this injection.

2.4.2 1d3v PIC

The discharge of the experiment has a cylindrical geometry. In the centre of the discharge the plasma does not see the edge of the electrodes and therefore no asymmetry effects may take place. For the middle of the discharge it is sufficient to do an one-dimensional approach. The velocity is still treated three-dimensional for energetic reasons.
The disadvantage of the 1d3v simulation is the neglect of different transport processes in radial direction. This leads to a discrepancy between simulation and real experiment. For example one has to choose a bigger electrode distance than in reality to get a comparable discharge as observed experimentally. Tests have shown that too little distances lead to very small bulks. That means that mainly sheaths and no real plasma in contradiction to the experimental observation are observed. I adjust my parameters in a way so that I receive comparable results close to one electrode, where the experimental measurements took place. In this case I cannot compare absolute values but can still see trends in distribution functions.
Still the asymmetric discharge can not be represented by an 1d simulation. Nevertheless, I

will use this method to get an idea of how the plasma will behave under this low pressure. I can compare these results with a 2d3v simulation. This will separate the asymmetric influence.

2.4.3 Parallelization

It takes a lot of time to run a simulation until the plasma is relaxed, usually up to 10^3 rf cycles. Equilibration in this context means that the macro quantities when averaged over one rf cycle do not change anymore.

Therefore, I will use the methods of parallelization especially 'Open MPI' (Message-Passing-Interface) [18]. The most time consuming part of this simulation is the particle pusher and calculating the collisions. If this task is split up onto several cores instead of one, the calculation time will decrease. It is intuitive to say that the particles should be divided equally onto multiple cores to get a faster code. If I order my particles in an array according to their position in the domain I will be able to split them up equally regarding our domain. I call it a particle induced domain decomposition. To generate output, however, it is important to reduce the macro-quantities to one core to get the whole information back together.

Knowing the advantages of parallelization one could naively say the more cores used the faster the simulation will get. But the time for the exchange of information between the cores like the potential, charge densities and surface densities rises with the number of cores exponentially. At some multiplicity of cores the message passing between the cores takes up more time than it would be saved by dividing the particles.

In table (2.2) the code is separated into different segments and the individual used time per 100 steps is measured.

In figure (2.10) the dependency of runtime on the number of cores is visualized. One can see that the runtime is not proportional to the number of cores and that the limit is reached at around 16 cores. Additionally, one step is divided into the different calculation parts to see which task scales good with the parallelization. One can observe that the collision and the pusher routine scale good with the domain decomposition. For the simulations mostly 4 cores are used, due to limited resources and efficiency. The overall limit would be different for runs with larger domains and different number of pseudo particles.

# cores	collisions	elastic collisions	electron pusher	ion pusher	solver
1	0.1304	0.7030	0.2160	0.0207	0.0011
4	0.0466	0.2570	0.0530	0.0051	0.0009
8	0.0349	0.2044	0.0261	0.0025	0.0009
16	0.0297	0.1881	0.0122	0.0012	0.0009
20	0.0306	0.1972	0.0085	0.0011	0.0009

Table 2.2: Benchmarks for parallelization optimization. All values are given in seconds.

Due to runtime problems I will mostly look at the one-dimensional simulations. The runtime until equilibration occurs in two dimensions for my system may take up to a few weeks
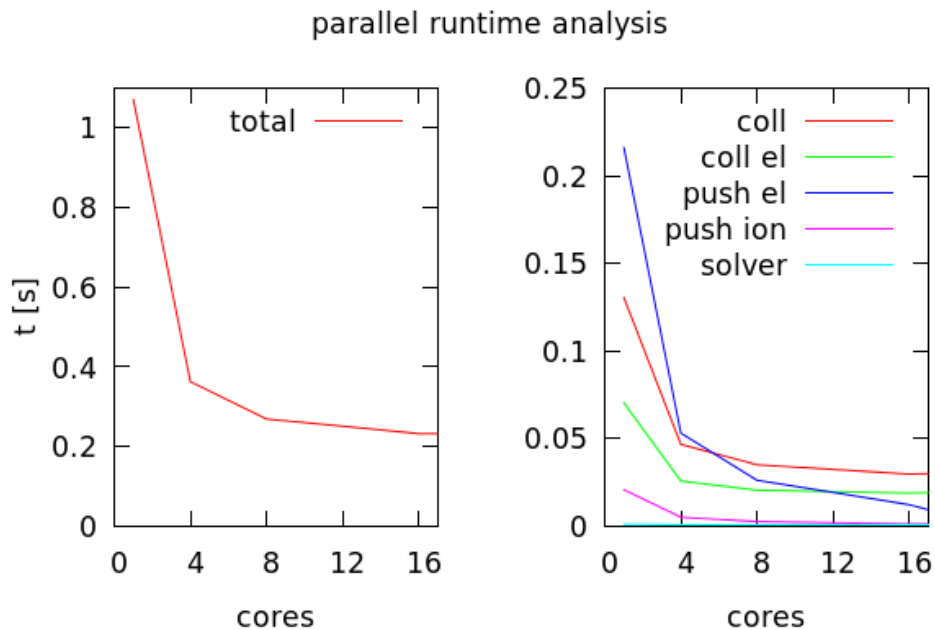
Figure 2.10: Runtime analysis depending on the number of used cores. On the left hand side the total time per step is shown. On the right hand side the runtime is divided into the different tasks (coll= plasma chemistry reactions, coll el= elastic coulomb collisions, push el= moving the electrons, push ion= moving the ions, solver= backsolve of the potenial) of one time step.

despite parallelization. Another approach to speed up the simulation is a parallel solver which uses techniques like successive over relaxation (SOR). At the moment this solver is not applied yet.

Now, all tools are together to do a microscopical study of electronegative ccrf discharges. I want to focus on the recent results of the group of Prof. Dr. Meichsner who measured highly energetic negative ions at the anode when using designated oxidized materials [4]. In the next chapter (2.5) I will shortly show the experimental setup and results. Afterwards, I will simulate an comparable discharge and compare the results.

2.5 Experimental setup

Experimental results from the group of Professor Meichsner are used. The experimental setup is shown in figure (2.11). It shows a schematic plasma chamber from above. The plasma apparatus consists of a cylindrical vacuum chamber built of stainless steel. At the cathode a rf voltage of frequency 13.56 Hz and a voltage of (500-2000) V is applied. The anode and the casing are both grounded. The distance between the electrodes is varied between (3-5) cm. The difference of the area of the cathode to the grounded anode in addition to the grounded wall leads to an asymmetric discharge characterized by a negative DC self-bias voltage at the powered electrode. The pressure is set up to (2-10) Pa and the process gas is oxygen O_2. To detect ions O^- at the anode a mass spectrometer is attached. Additionally, a PROES (**P**hase **r**esolved **o**ptical **e**mission **s**pectroscopy) diagnostic is applied.

Operating parameter:

frequency :	13.56 MHz
power :	7...51 W
pressure :	4...10 Pa
process gas :	O_2
material of electrode :	stainless steel, SiO_2, Al_2O_3, MgO
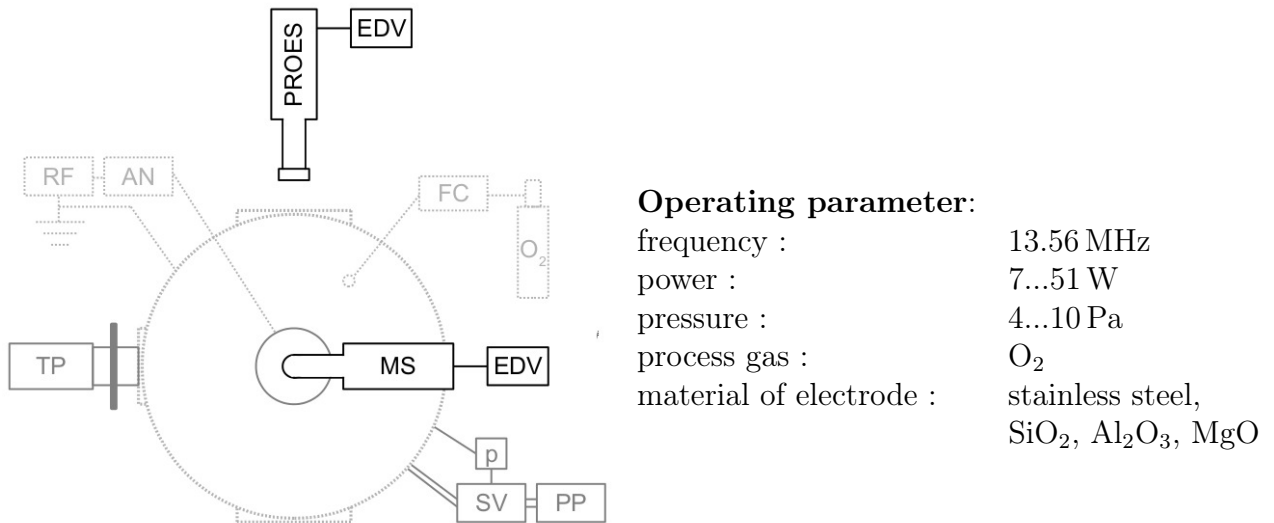
Figure 2.11: Top view of the schematic experimental setup taken from [4].

By applying a voltage to the cathode a plasma develops. The basics of ccrf plasma physics are described in chapter (2). The cold positive ions $O_2{}^+$ of the bulk get accelerated at the plasma sheath towards the grounded anode. There they are detected by the mass spectrometer and result in a well known distribution [3] as shown in figure (2.12). The incoming negative ions O^- are detected as well. The number of detected negative ions is much lower than the number of detected positive ions. The negative ion distribution of stainless steel and magnesium oxide in figure (2.13) show a low-energy peak followed by a plateau which proceeds up to very high energies of several 100 eV.
Depending on the cathode material a high-energy peak appears in the negative ion distribution.

In this experiment different materials have been tested (SiO_2, Al_2O_3, magnesium oxide (MgO), stainless steel). In the following I use a PIC simulation to test if these ions originate from surface processes at the cathode or if they emerge from asymmetry effects.
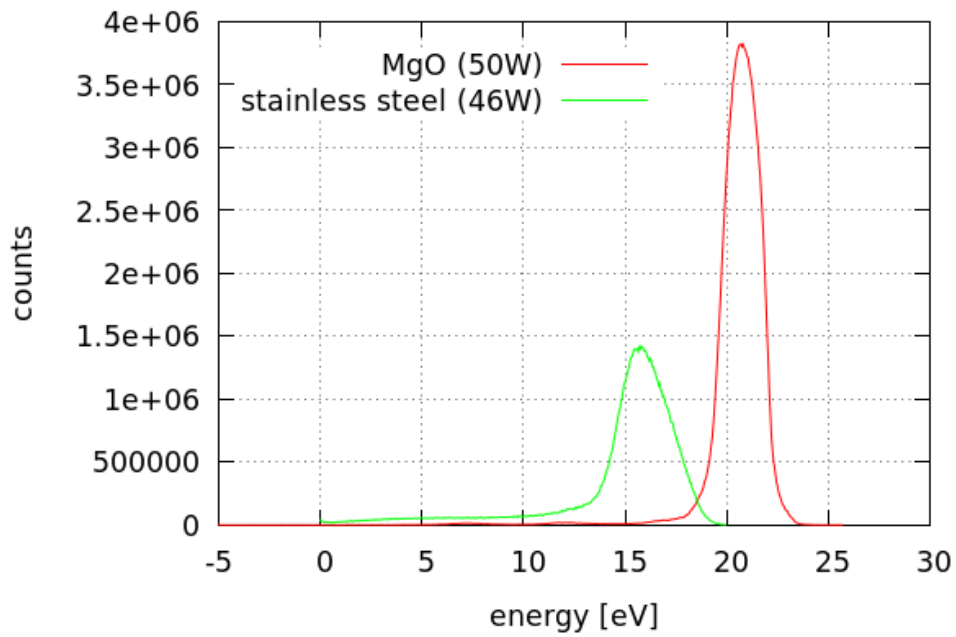
Figure 2.12: Comparison of the positive ion energy distribution for stainless steel and magnesium oxide.
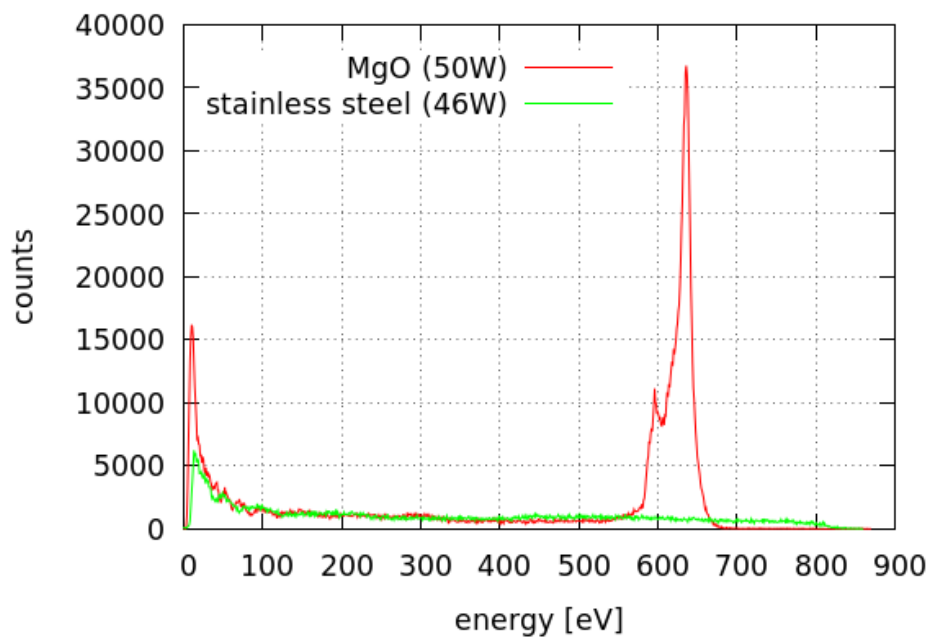
Figure 2.13: Comparison of the negative ion energy distribution for stainless steel and magnesium oxide.

3 PIC simulation of a ccrf discharge

With the PIC method I simulate the previously described capacitively coupled radio frequency discharge. The system starts with a pressure of $10\,\mathrm{Pa}$ and a peak-to-peak voltage of $800\,\mathrm{V}$. The moderate pressure ensures a stable discharge. From there on the pressure will be reduced to get to low pressures around $2\,\mathrm{Pa}$. The radio-frequency is set to $13.56\,\mathrm{MHz}$. The initial values for the considered electron density $n_e = 5 \cdot 10^9\,/\mathrm{cm}^{-3}$ and electron temperature $T_e = 4\,\mathrm{eV}$ are set which lead to a super particle factor of about 6000 .
This leads to a Debye-length of $\lambda_{Db} \approx 0.021\,\mathrm{cm}$ and an electron plasma frequency of $\omega_{pe} \approx 3.99 \cdot 10^9\,\mathrm{s}^{-1}$. Hence follows the spatial resolution

$$\Delta x = \lambda_{Db}/2 \approx 0.0105\,\mathrm{cm}\ , \tag{3.1}$$

$$\tag{3.2}$$

and the time step

$$\Delta t = 0.2\frac{1}{\omega_{pe}} \approx 5.01 \cdot 10^{-11}\,\mathrm{s}\ . \tag{3.3}$$

$$\tag{3.4}$$

The electrode gap of the experiment is $5\,\mathrm{cm}$. Tests have shown that if the domain is chosen that small the resulting bulk is too small. Hence, no sufficiently big plasma to simulate the dynamics exists. This is due to the missing radial transport processes which will be included in a two dimensional simulation. The number of cells $n_{cell} = 640$ is set resulting in a domain length of $6.72\,\mathrm{cm}$.

One rf cycle takes up to $N_{rf} = \frac{1}{\Delta t \cdot 13.56\,\mathrm{MHz}} \approx 1470$ steps. As already discussed it takes up to 10^3 rf cycles for the plasma to get to an equilibrated state. That means one has to calculate at least $1.5 \cdot 10^6$ steps. I will always consider a pure oxygen plasma.

3.1 Studies of low pressure discharges

The resulting potential and density distributions for $p = 10\,\mathrm{Pa}$ and $U_{rf} = 800\,\mathrm{V_{pp}}$ are shown in figure (3.1).

One can see how the densities build a plasma bulk with electrons, positive ions and negative ions. Further, the sheaths are visible, where a positive space charge exists. The sheath width here is about $50\lambda_{Db}$ which equals $\approx 1\,\mathrm{cm}$. I am interested in the energy distribution
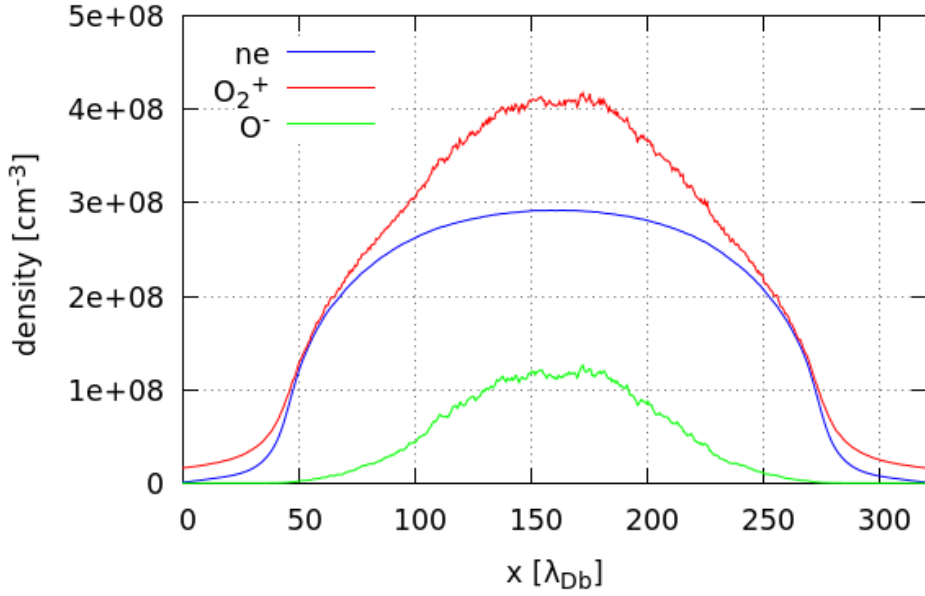
Figure 3.1: Density distribution of e^-, O_2^+ and O^- at $10\,\mathrm{Pa}$ and $800\,\mathrm{V_{pp}}$.

functions of the species, especially the of O^-. In figure (3.2 and 3.3) the energy distributions of the positive and negative ions are shown. The figures show the number of ions on a logarithmic scale as a function of their energy in electron volt and their position in the discharge in multiples of λ_{Db}. At 0 the anode and at $320 \cdot \lambda_{Db}$ the driven cathode is located.

Both energy distributions of O_2^+ and O^- (figure 3.2) show the expected behavior of cold ions in the center of the discharge ($50 - 270 \cdot \lambda_{Db}$) and their acceleration in the sheath. The energy of O_2^+ at the electrodes coming from the bulk is accordingly equal to the energy they get from the potential drop $\Delta\Phi$. The lower energy tail results of elastic collisions with O_2 and ionization processes in the sheath.

The energy distribution of O^- is similar to the distribution of an electron energy distribution (3.4) as they behave just like heavy electrons. But, there are also some ions of higher energy. One can see that they originate from the sheath. To have a better understanding of the production rate of O^- I have a look at the dissociative attachment processes (figure 3.5). This production rate looks similar to the distribution of the electron density. I see that most ions are produced in the bulk where they stay relatively cold. But a few are produced in the sheath. These are the ones responsible for the high-energy tail of the energy distribution function.

The simulated energy distribution is similar to the one from the experiment. Both have a high count-rate at low energies descending into a high-energy tail which cuts off at around half of the peak-to-peak voltage (s. figure (3.2)).

The density ratio between electrons and negative ions at a pressure of $10\,\mathrm{Pa}$ and a driver voltage of $U_{pp} = 800\,\mathrm{V}$ is about $\alpha \approx 0.3$. Since I am interested in electronegative states the pressure has to reduced further to attain a true electronegative plasma. This case will be taken as a comparison to the lower pressure results.

In figure (3.6) the density distribution of $2\,\mathrm{Pa}$ is shown.
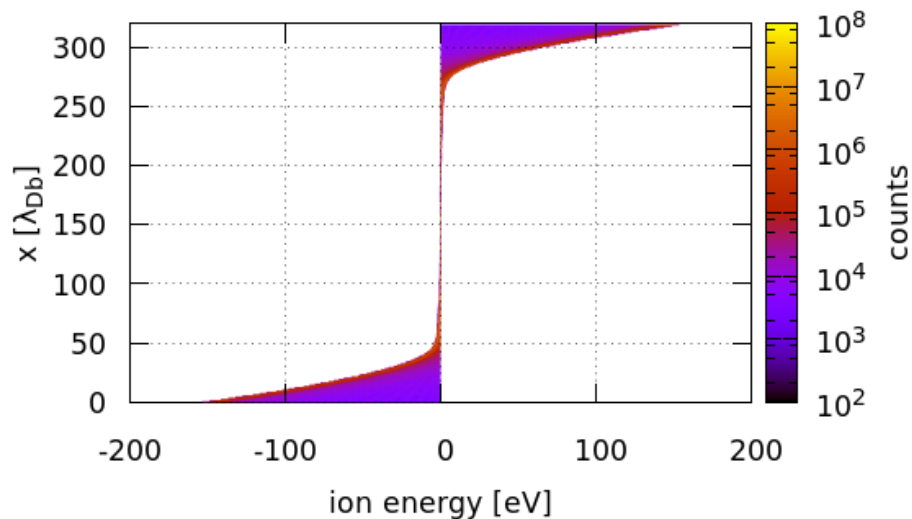
Figure 3.2: Logarithmic Energy distribution of positive ions O_2^+. Simulation parameters were set to a pressure of $p = 5\,\mathrm{Pa}$ and a voltage of $U_{rf} = 800\,\mathrm{V_{pp}}$.
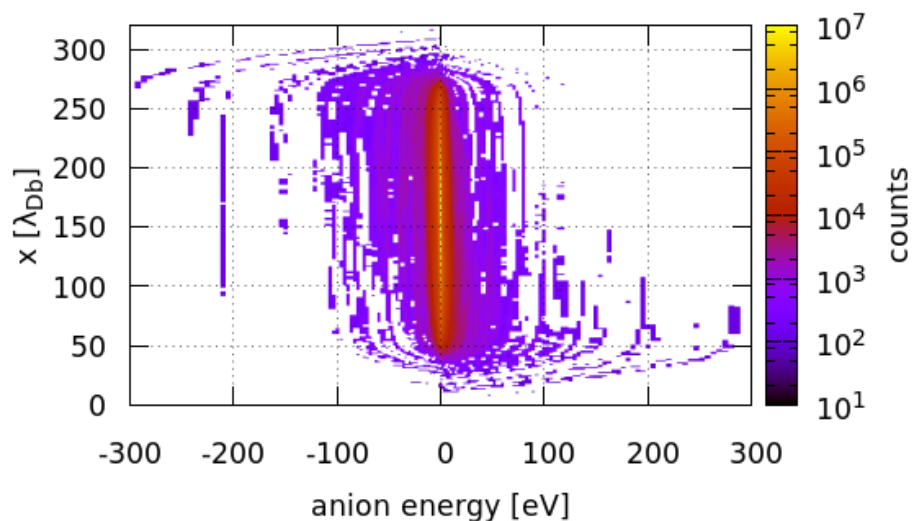
Figure 3.3: Logarithmic energy distribution of negative ions O^-. Simulation parameters were set to a pressure of $p = 5\,\mathrm{Pa}$ and a voltage of $U_{rf} = 800\,\mathrm{V_{pp}}$.
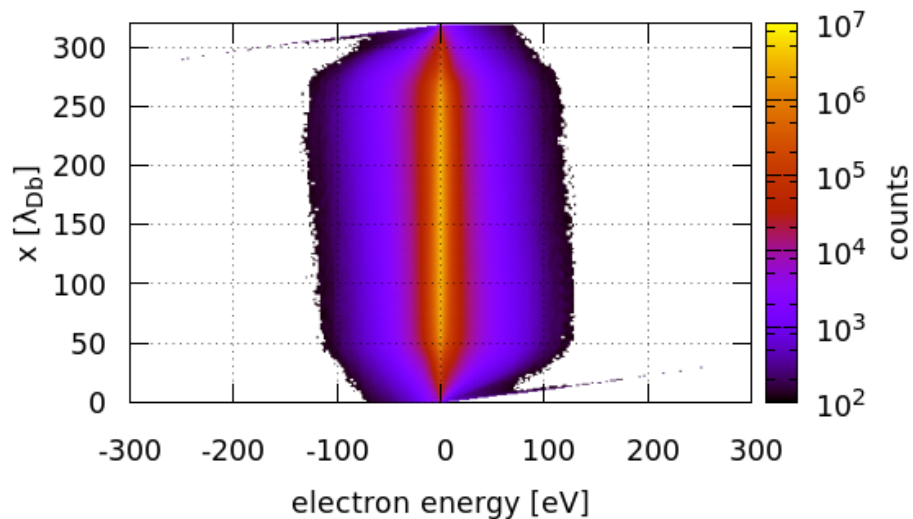
Figure 3.4: Logarithmic energy distribution of electrons. Simulation parameters were set to a pressure of $p = 5\,\mathrm{Pa}$ and a voltage of $U_{pp} = 800\,\mathrm{V}$.
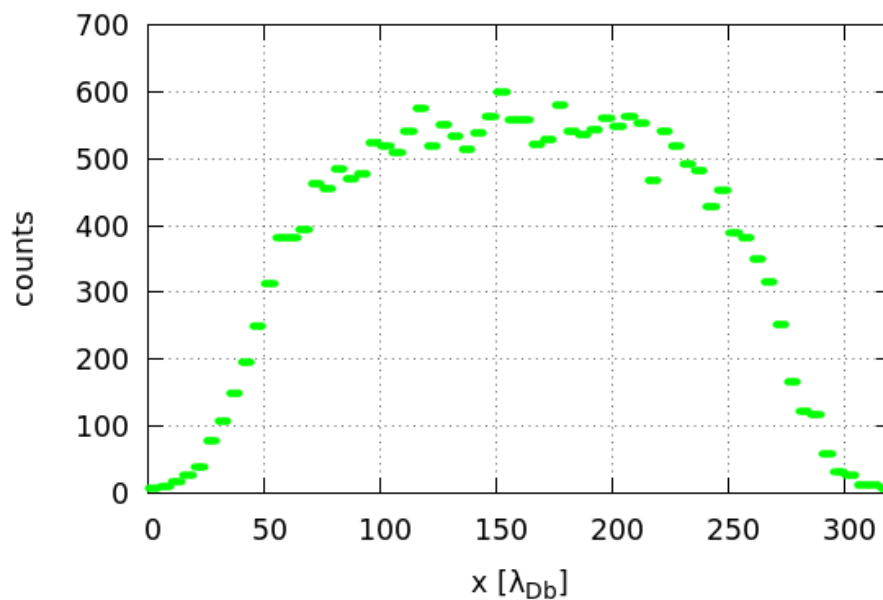
Figure 3.5: Total numbers of dissociative attachment processes per 10^5 steps per cell implying the production rate of O^-.
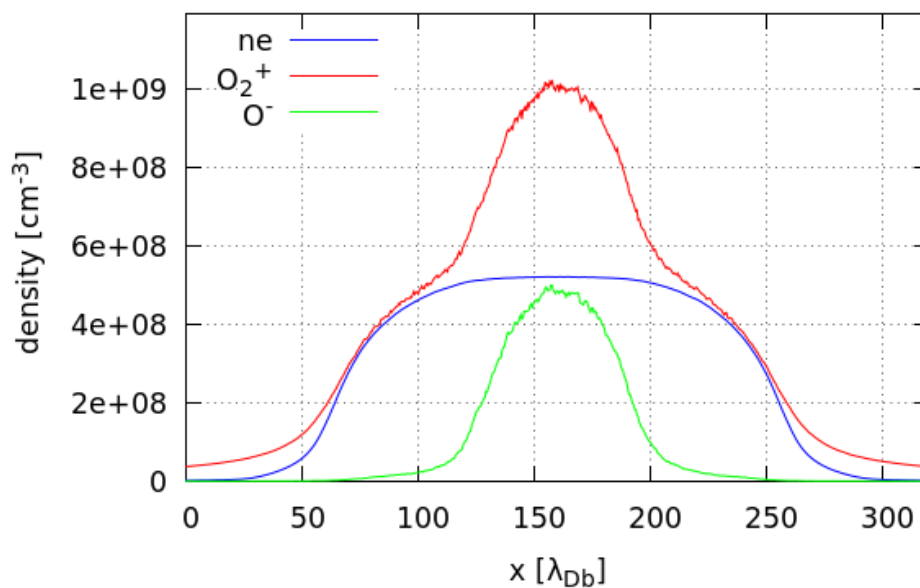
Figure 3.6: Density distribution at lower pressures (2 Pa). The driver voltage was set to $U_{rf} = 800\,\mathrm{V_{pp}}$.

The number density of negative ions rises when the pressure falls. It is apparent that at these pressures the plasma is close to an electronegative state. But looking at the energy distribution functions (s. figure 3.7) no big difference is seen.

The results for low pressure discharges do not give us an explanation for the measured high-energy peak (s. figure 2.13).
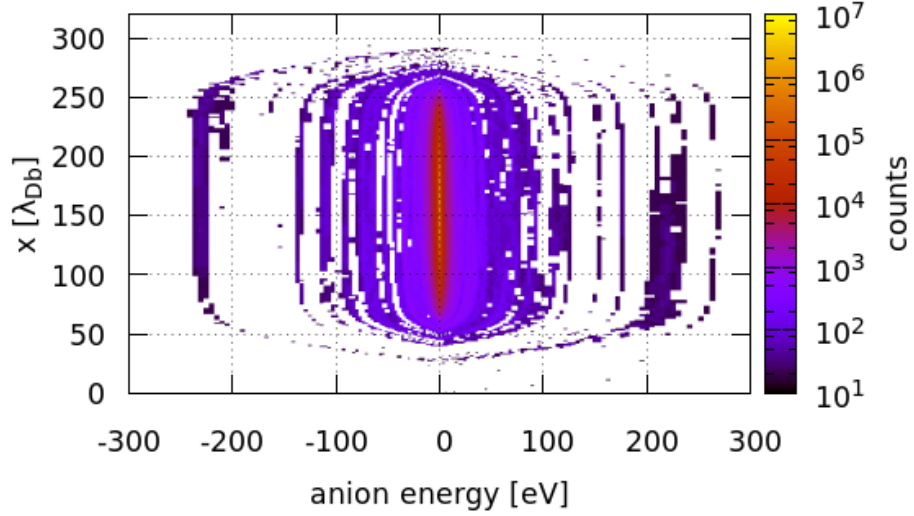
Figure 3.7: Logarithmic O^- energy distribution at lower pressure ($2\,\mathrm{Pa}$). The driver voltage was set to $U_{rf} = 800\,\mathrm{V_{pp}}$.

3.2 Discharge with secondary ion emission

With the proposed SIE injection model of oxygen anions the simulation is redone. In figure (3.8) one can see that the number density of the anions is higher and slightly shifted towards the cathode. This is due to the additional asymmetric injection process of SIE at the cathode. I could also apply the SIE to the anode but as in the experiment the oxide is usually just placed at the driven cathode. Here, $\eta = 0.03$ is chosen.

Since I want to study the behavior of the anions coming from the surface I separated the two species. I refer to them as anions produced by volumetric processes in the plasma O_p^- and surface anions O_s^-.

It is visible that the density distribution of O_s^- is of one magnitude higher than O_p^-. This depends on the chosen injection ratio η. The surface ion density has a peak close to the cathode resulting from the injection of O_s^-. In addition a small density peak at the sheath edge in front of the cathode is noticeable. It forms due to elastic collisions of the anions O_s^- in the sheath as explained below.
Looking at the energy distribution of O_s^- (s. figure (3.9)) one sees that they get accelerated by the sheath potential. Here I just look at the ions produced by surface effects because the anions produced by volumetric processes are already treated. After passing the bulk the O_s^- get reflected in the anode sheath similar to electrons.
  An high-energy peak builds up. It decays with the time of flight due to charge-exchange and elastic collisions with neutral molecules O_2 which results in an energy loss for the anion. Also a part of the anions gets detached by neutrals or recombines with positive ions.
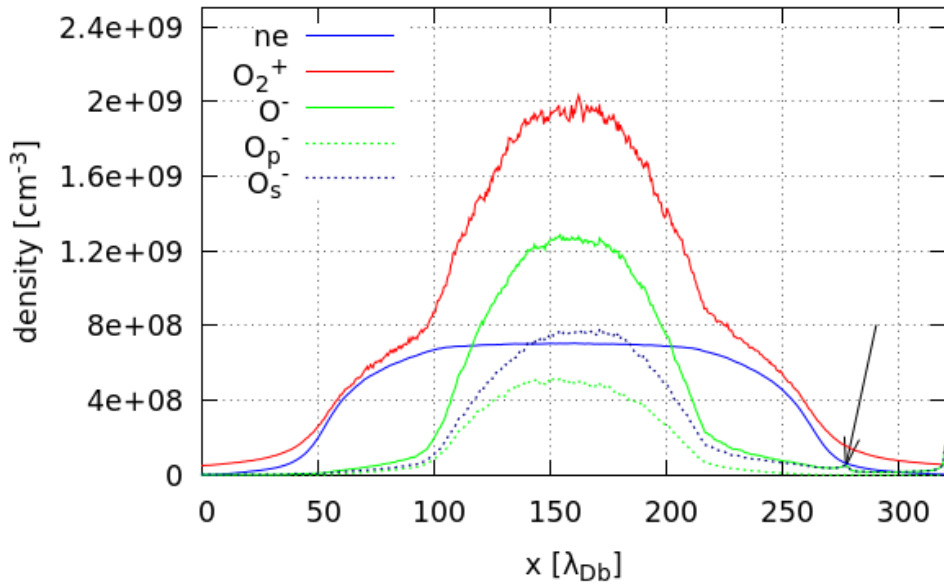
Figure 3.8: Density distribution of e^-, O_2^+ and O^- with secondary ion emission at the cathode ($\eta = 0.03$). The pressure was 5 Pa and the rf power was set to $U_{rf} = 800\,\mathrm{V_{pp}}$. The arrow marks the little density peak of O_s^- at the cathode sheath edge.
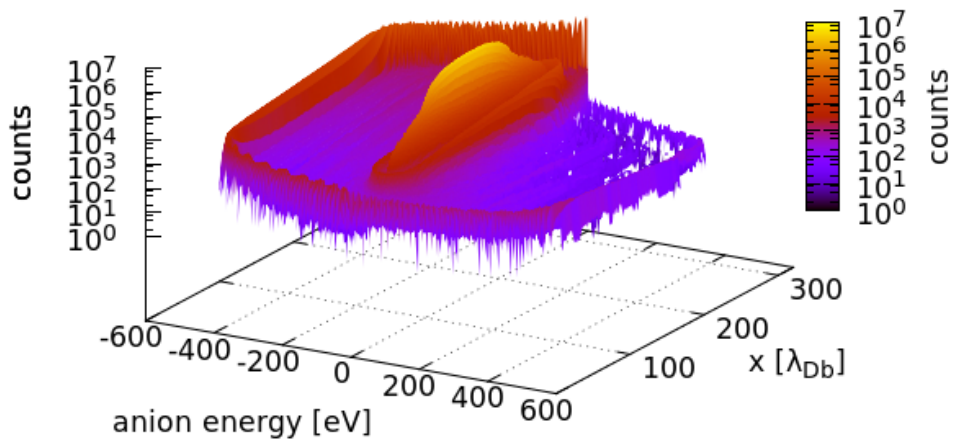
Figure 3.9: Logarithmic energy distribution of surface anions O_s^- at $p = 5\,\mathrm{Pa}$ and $U_{pp} = 800\,\mathrm{V}$ averaged over 10^5 rf cycles. The injection ratio was $\eta = 0.03$.
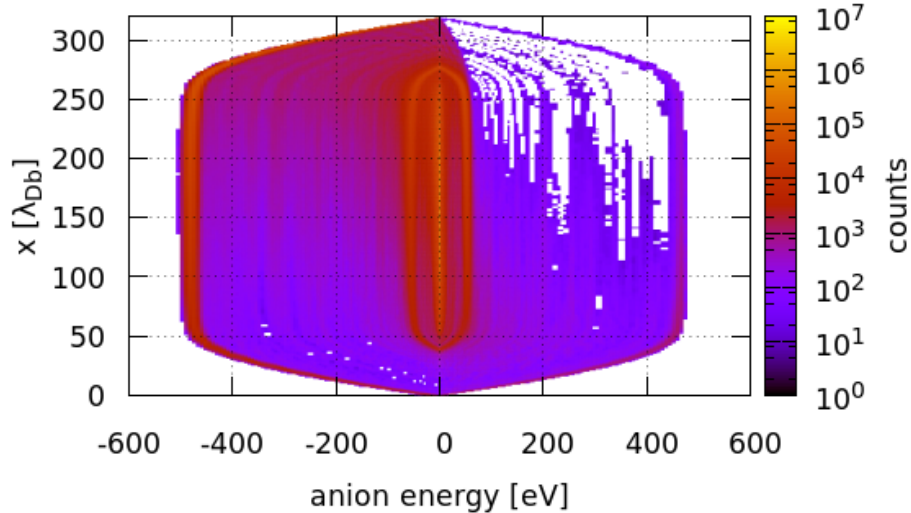
Figure 3.10: Same energy distribution as in figure (3.9) shown from the top.

Until now it was assumed that if an anion collides with a neutral it almost gets detached every time. But the anions also do elastic collisions which leads to an energy loss and a plateau in the energy. After a certain time of flight the anions get cold through collisions and stay in the bulk. There, their distribution does not differ from the anions produced by volumetric processes O_p^-. In figure (3.11) the difference between the collision numbers for a normal discharge and a discharge with additional SIE are shown. The cathode is still located at $320 \cdot \lambda_{Db}$. As expected for the bulk anions O_p^- there is no difference in the numbers of elastic collisions. Most elastic collisions happen in the bulk while the sheaths are mostly collisionless. But for the surface ions O_s^- one can see that the collisions in the cathode sheath cannot be neglected. They lead to an energy loss for the anions which impacts on their energy distribution.

In figure (3.10) a structure in the lower energy area can be seen. The negative ion energy distribution depends on the phase of the rf cycle when the particles enter the sheath, since the potential is rf modulated. This and the performed elastic collisions during this phase lead to a peak structure in the ion energy distribution. For positive ions the behavior in rf sheaths is well studied. Depending on the ratio of the ion transit time τ_{ion} and the applied power frequency τ_{rf} the ion energy distribution at the cathode shows saddle like peak structures. For further information on positive ions in rf sheaths I refer to [19]. But for negative ions the microscopic dynamics are not well studied yet. To get an impression of the dynamics in the sheath the phase resolved energy distribution for O_s^- is shown in figure (3.14)).

The density peak at the sheath edge (as seen in figure (3.8)) originates from the low-energy peak in the energy distribution. To understand this structure I calculate how long an anion stays in the sheath. Therefore the approximate transit time of an anion τ_{ion} and the rf-cycle time τ_{rf} are needed. For the transit time τ_{ion} an average ion energy of $40 - 50\,\text{eV}$ and a traveled distance of $\approx 1\,\text{cm}$ is assumed, which is approximately the sheath width.
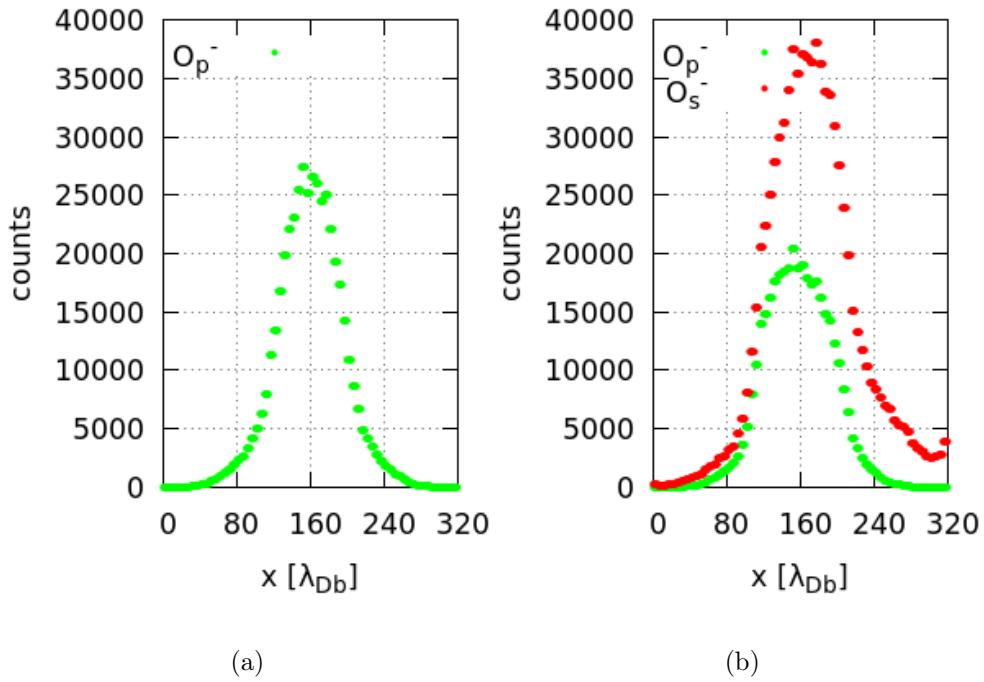
Figure 3.11: Number of elastic collisions of negative ions O^- with neutral molecules O_2 per 10^5 steps. The figure shows them in simulation without SIE (a) and with SIE ($\eta = 0.03$) (b) where between the two O^- species is differentiated.

The ratio

$$\frac{\tau_{ion}}{\tau_{rf}} \approx 4.5 \tag{3.5}$$

gives us the number of rf cycles an anion stays in the sheath. Hence the number of peaks in the ion energy distribution must be similar. In figure (3.9) one can see a high-energy peak and 4-5 low-energy peaks in the bulk region. The formation of these density waves is shown in figure (3.14). The rf power is positive in the first half of the rf cycle and hence the anions get less rejected of the electrode because the potential drop is smaller. So they can enter the sheath even with comparable low energies. In the second half of the rf cycle the applied voltage is negative and hence the anions get more rejected due to the bigger potential drop. Over one rf cycle a saddle like structure with multiple peaks in the sheath builds up. At the sheath edge these density waves overlay. This explains the density peak at the sheath edge.

For comparison in figure (3.13) an equal discharge is shown without elastic collisions between O^- and O_2. The distribution reduces to the cold bulk anions and the high-energy peak. That means that the building of the energy plateau of the anions is mainly influenced by elastic collisions. The cold ions in the bulk are produced by charge exchange collisions where the resulting anion is cold. Hence, there are no anions in the energy area between the cold bulk ions and the fast anions which do not react with other particles and just follow the electric field.
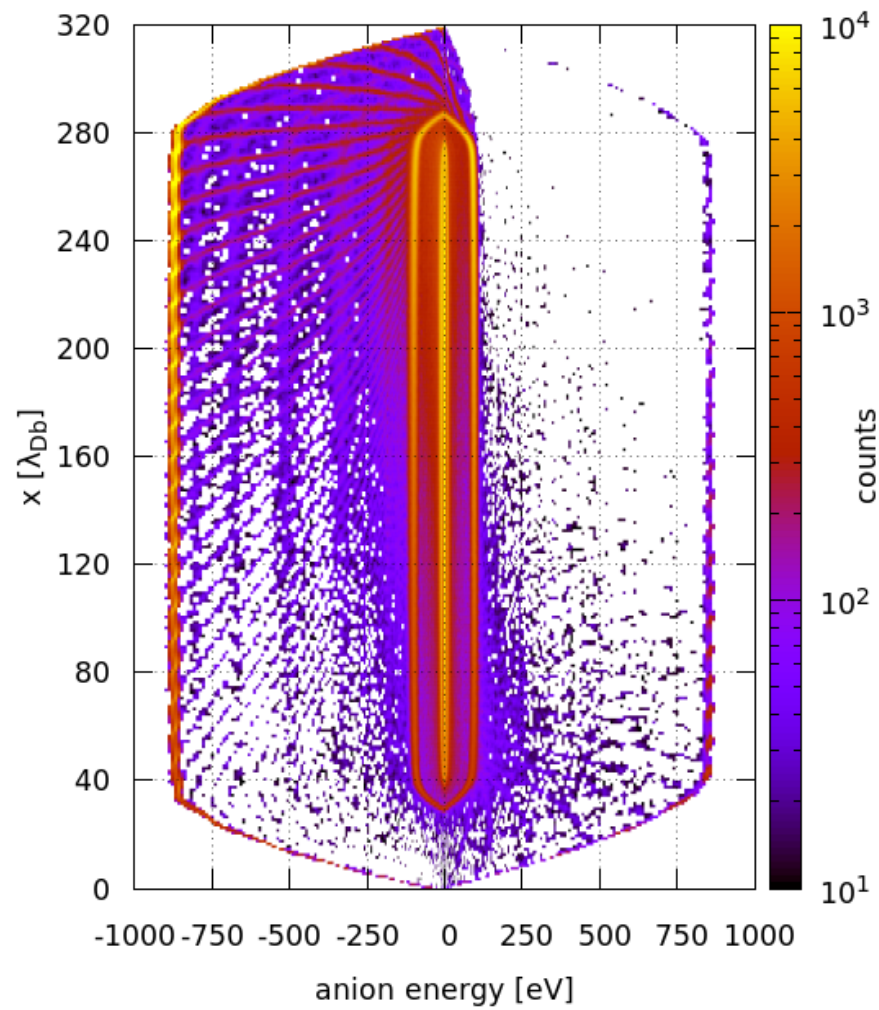
Figure 3.12: Same energy distribution as in figure (3.10) at t=0 of the rf cycle, which is equal to $U(t) = 0$.
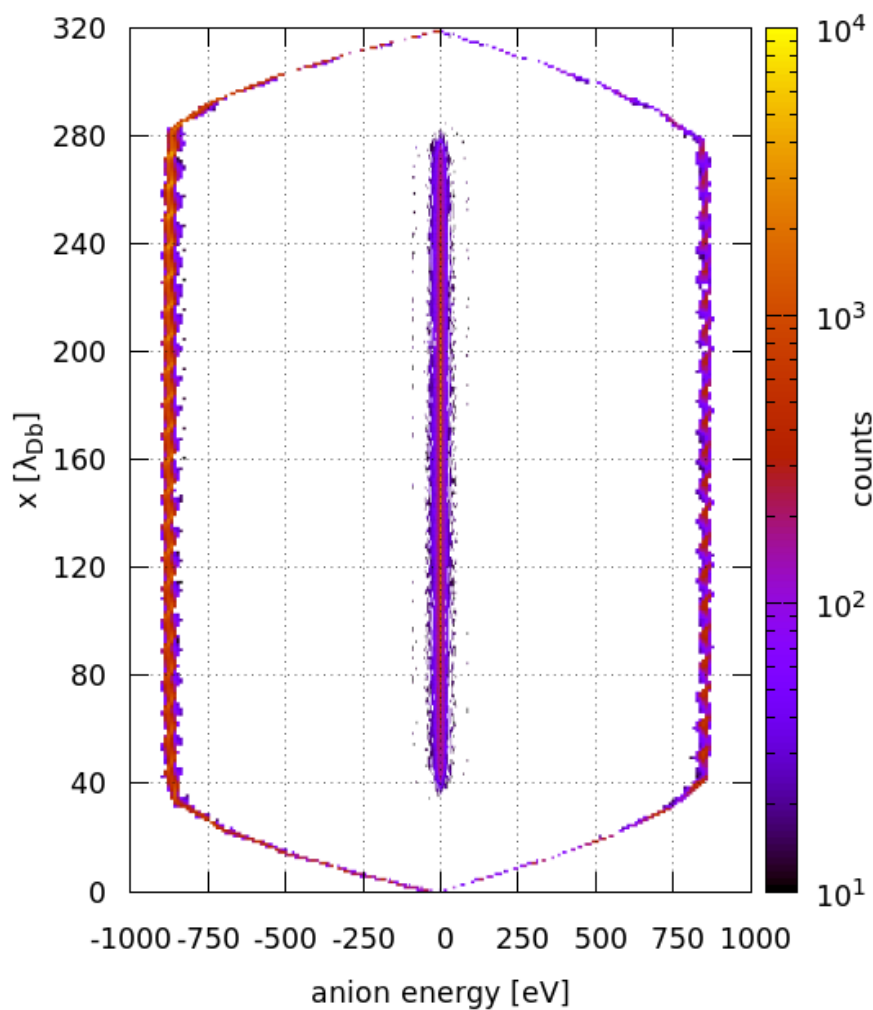
Figure 3.13: Phase resolved energy distribution of O_s^-, simulated without elastic collisions, at t=0 of the rf cycle, which is equal to $U(t) = 0$. The parameters were $p = 5Pa$ and $U_{rf} = 1600\,\mathrm{V_{pp}}$.
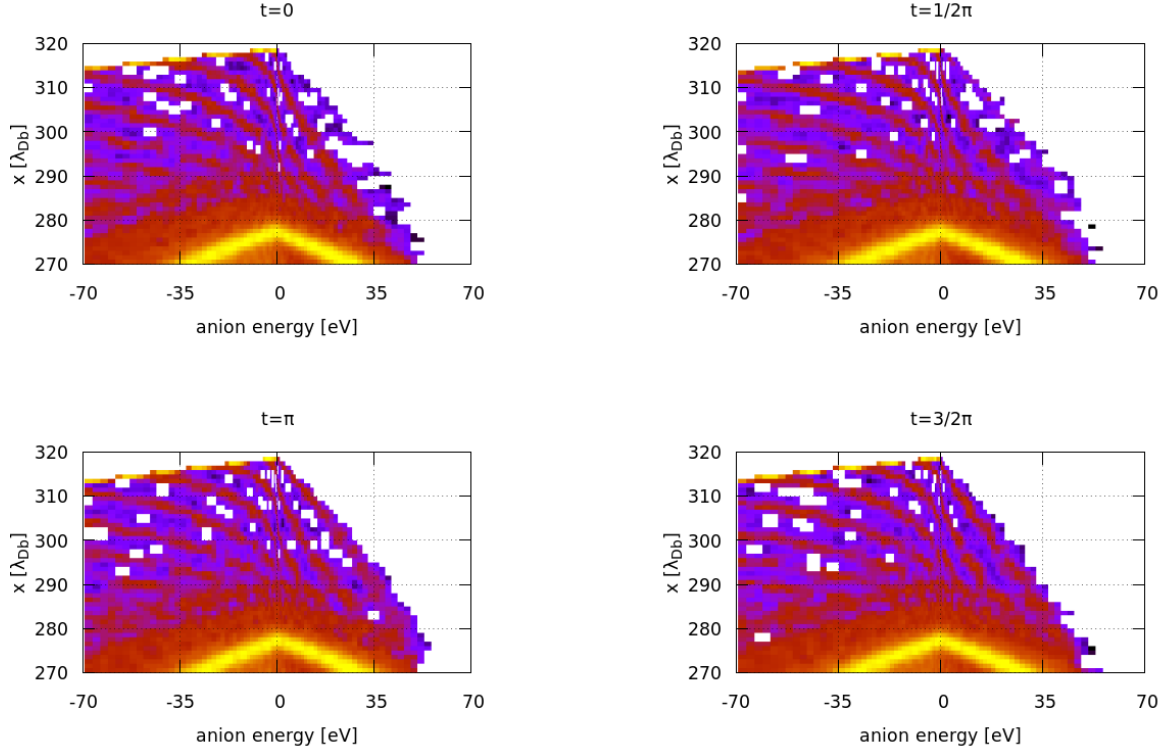
Figure 3.14: Phase resolved energy distribution of the anion O^- energy distribution at different phases of the rf cycle. The distribution is given at $\psi{=}0$ ($U_{rf}{=}0\,\text{V}$), $\psi{=}\frac{1}{2}\pi$ ($U_{rf}{=}400\,\text{V}$), $\psi{=}\pi$ ($U_{rf}{=}0\,\text{V}$) and $\psi{=}\frac{3}{2}\pi$ ($U_{rf} = -400\,\text{V}$).

Now that the formation of the negative ion energy distribution is understood the results can be compared with the ones from the experiment. In the one dimensional model the anions do not reach the anode. This is due to the symmetric averaged potential. In the experiment where the cathode potential is shifted by the self-bias voltage the resulting potential is asymmetric (s. figure (2.4)). That means, the anions get enough energy to get to the anode while in the current simulation they get reflected by the sheath potential. Thus, to compare my results I have to cut through the energy distribution at the sheath edges (s. figure 3.15).

Both distributions look similar (s. figure (3.15)). This confirms that negative ions produced at the surface may lead to the measured high-energy peak. But the energy distribution function of the simulation has low energy peaks (at $< 100\,\text{eV}$), too. These peaks are not observed in the experiment. I consider them to be created due to the lack of asymmetry in the simulation. Because in one dimension there is no self-bias voltage and the anion energy is not high enough to get to the anode. Instead, they get reflected and hence build up the described lower energy peaks through the rf and elastic collisions. In the experiment all high-energy anions are detected and thereby removed of the discharge.

Now the system was prepared with SIE and gave a qualitative description of the discharge. The simulation results are close to the experimental results. In the following the pressure, the power of the electrode and the injection coefficient η are varied to get a more quantitative description.
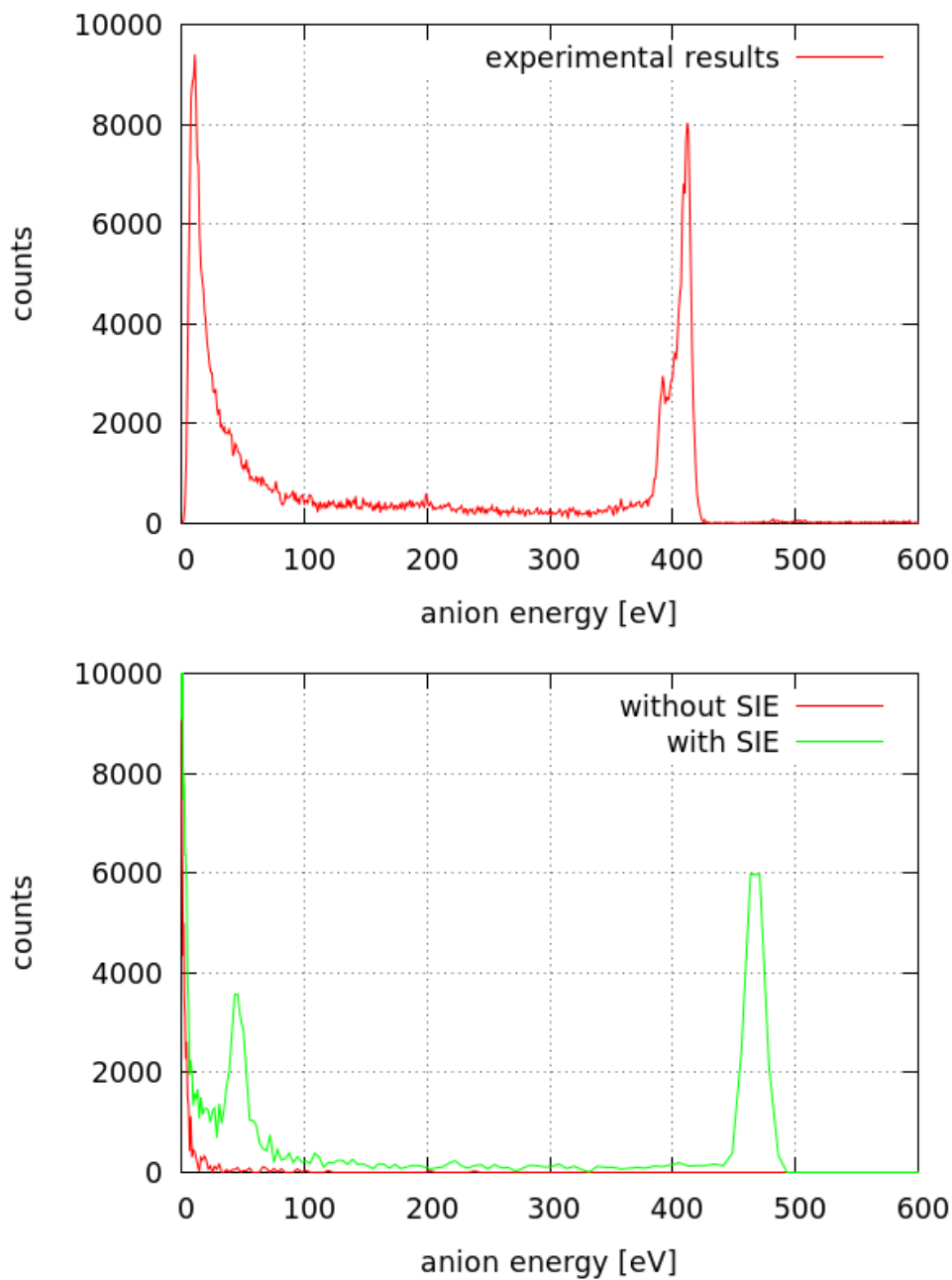
Figure 3.15: Energy distribution of negative ions O^-. Top: Experimental results for MgO measured at the anode for different rf powers. Bottom: Simulation result with 1d3v PIC simulation with additional SIE taken at the anode sheath edge.

4 Parameter analysis of anion energy distributions

In this chapter a quantitative description of the surface anion O_s^- energy distribution in a low temperature low pressure oxygen ccrf discharge is given through PIC simulations. I will show the dependence on pressure p, applied rf power U_{rf} and the SIE injection parameter η. Here, the SIE method developed in chapter (3) is always used. All energy distributions in this chapter are taken at the anode sheath edge to compare them with experimental results.

4.1 Cathode power variation

First different rf powers U_{rf} in a range of $400-1600\,\mathrm{V_{pp}}$ are applied. The potential drop $\Delta\Phi$ will adjust to the applied voltage. Hence, the ions should be accelerated more with higher rf powers. In figure (4.1) the resulting energy distributions are shown. The high-energy
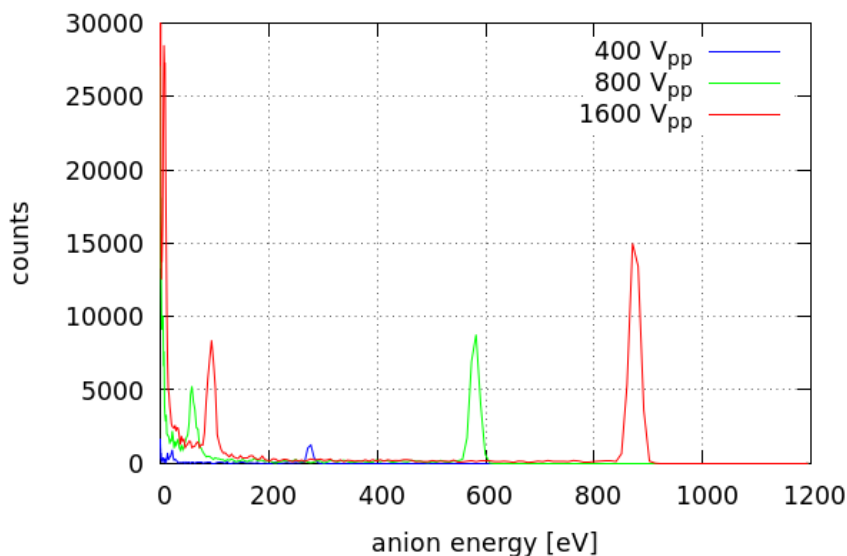
Figure 4.1: O_s^- energy distribution under different driver voltages U_{rf} with $5\,\mathrm{Pa}$ and $\eta = 0.01$.

peak is located around $\frac{1}{2}\,\mathrm{V_{pp}}$. Also, the count rate rises for higher voltages due to the larger mean free path of faster anions. The probability of getting detached is reduced with increased energy of the anion (see cross sections for detachment in figure (2.9)).
These results are close to the experimental measured distributions.

4.2 Injection ratio η variation

Now, the dependency of η is studied. As a reminder η describes the ratio of the number of incoming positive ions to the number of emitted anions $\frac{n(O_s^-)}{n(O_2^+)}$. Comparing with the experiment the size of η should be about 1%, which is also applicable for the secondary electron emission. η will be varied in a range of $0.005 - 0.03$ avoiding the critical area of too high injection coefficients. The variation of η equals different work functions in the cathode material. So it is depending on the used material. The experiment shows that the count rate of high-energy ions depends on the used material. The simulation results are shown in figure (4.2), where the pressure was set to $5\,\mathrm{Pa}$ and the power to $800\,\mathrm{V_{pp}}$.
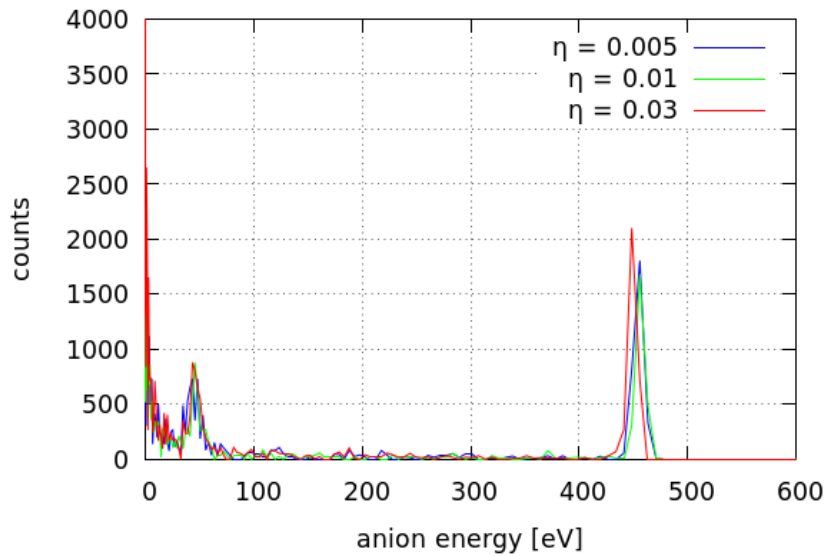
Figure 4.2: O_s^- energy distribution for different η with $5\,\mathrm{Pa}$ and $U_{rf} = 800 V_{pp}$.

The distribution is not influenced much by the variation of η in the chosen parameter range. This is not supported by the experiment. The explanation is again the symmetry of the one-dimensional discharge which keeps the surface ions in the discharge. Hence they can fly multiple times through the plasma and after equilibration a constant anion flux builds up, which depends only weakly on the emitting ratio η. But the injection parameter has an influence on the density distributions since it is an additional source of negative ions. These influences lay beyond the scope of this thesis and may be discussed in later works.

4.3 Pressure variation

The pressure is varied in a range of $2 - 10\,\mathrm{Pa}$. The count rate of highly energetic ions will rise with lower pressure because less collisions take place which could lead to energy loss or detachment. The other conditions were set to $U_{rf} = 400\,\mathrm{V}$ and $\eta = 0.01\,\mathrm{V}$. In figure (4.1) the energy distributions for different pressures are shown.

As expected the count rate of highly energetic ions rises with falling pressure while the energy itself does not change. The same dependency is detected in the experiment.
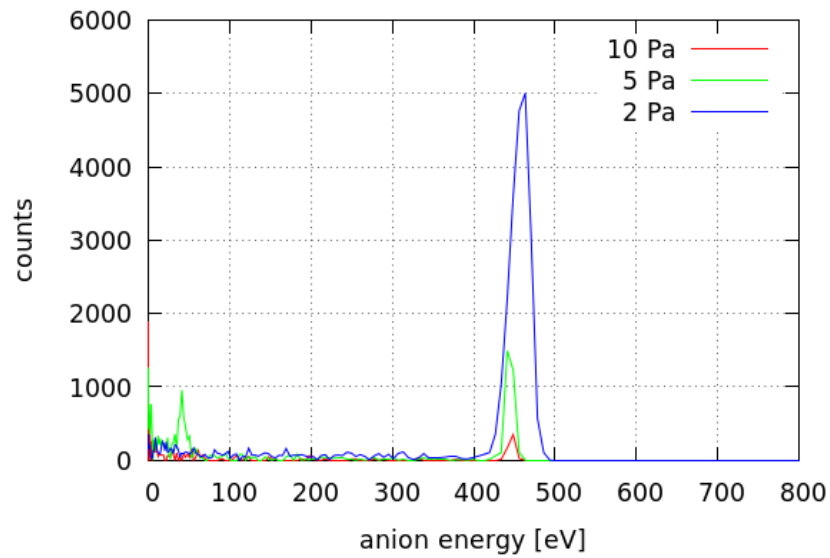
Figure 4.3: O_s^- energy distribution under different pressures with $U_{pp} =$ V and $\eta = 0.01$.

Thus, a quantitative study of the anion energy distribution behavior is given in relation to pressure, power and injection variation. All this was done with a one dimensional model which is just an approximation for the center of the discharge. To simulate an asymmetric discharge at least two dimensions have to be taken into account.

5 Two-Dimensional PIC simulation

The two-dimensional PIC code used was developed by the group of Prof. Dr. Ralf Schneider. Over several years the code was developed and optimized for ion thruster modeling. I adapted it to simulate a capacitively coupled rf discharge.

Due to the symmetry of the discharge a cylindrical geometry in r and z direction is used. Since this geometry is not cartesian the cell volume increases in r direction. To consider this the particles have to be weighted when calculating the charge density according to their distance to the axis $\sim \frac{1}{r}$. The geometry used is shown in figure (5.1).
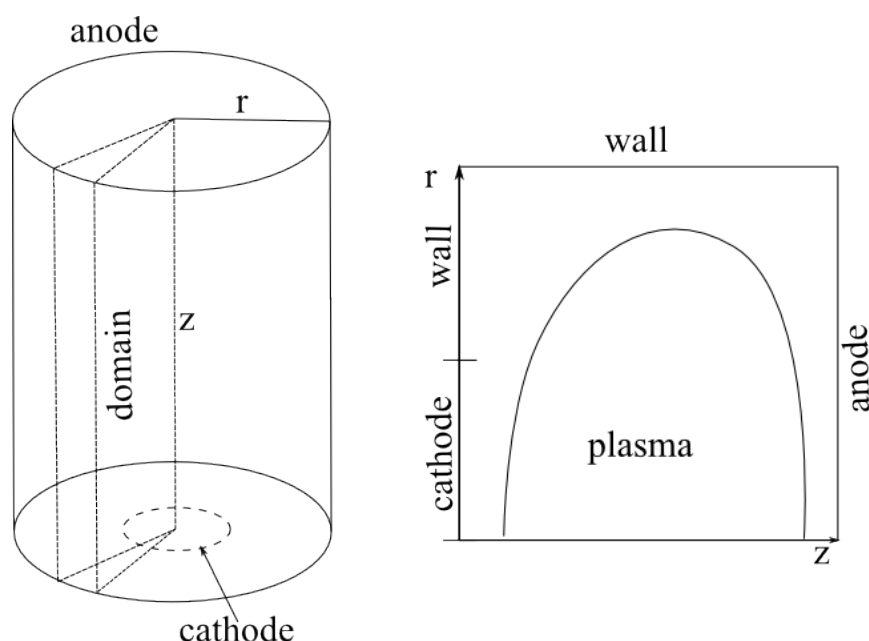
Figure 5.1: Schematic figure of the geometry of the discharge. On the left hand side is shown the whole discharge in a cylinder, where the simulation domain is marked as a slice. On the right hand side the resulting domain with the corresponding boundary conditions is shown.

To realize an asymmetric discharge the size of the cathode is set smaller than the size of the anode. This in addition to the grounded wall leads to a strong asymmetry. In an asymmetric discharge the high mobility of the electrons charges the cathode, which then gets a negative self-bias voltage. Therefore the particles impinging the cells in front of the cathode are counted. There they are summed up and then equally distributed onto the cathode, since a metallic surface is assumed. As a side remark a dielectric discharge would be also possible. Then, the surface charge would not be averaged, but kept local.

A problem occurring in two dimensions is the radial loss of particles. The production rate of ions and electrons must be higher then in one dimension.

5.1 Micro discharge

To get a feeling for basic asymmetric discharges argon as a working gas is used, because it ensures a more stable discharge than oxygen.

To realize the parameters of the experiment, which uses electrode radii of a few centimeters, the domain gets big (>500x500 cells). I will restrain myself to smaller domain sizes due to runtime reasons and try to get to stable discharges, beginning with a micro discharge.
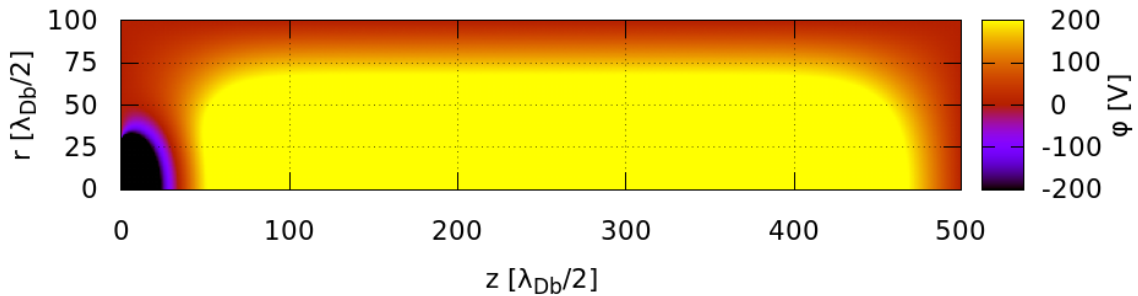
Figure 5.2: Potential of a 2d discharge with an asymmetry ratio of $\frac{A_{cathode}}{A_{anode}} = 0.3$ with argon as an operating gas. On the left hand side is the driven cathode and on the right hand side is the grounded anode. The wall at the top is grounded. The pressure was set to $\approx 1\,\mathrm{Pa}$ and the applied rf power was $2000\,\mathrm{V_{pp}}$.

Therefore, a cathode with a radius of $3\,\mathrm{mm}$ and an anode with a radius of $1.05\,\mathrm{cm}$ is taken and a grounded box is put around it. The electrode gap is about $5.25\,\mathrm{cm}$. The resulting potential is shown in figure (5.2). On the lower left side the powered cathode is located and the other walls (boundaries) are grounded.

Because the walls are grounded the sheath in front of the side wall should be as big as in front the anode. Looking at figure (5.2) both sheaths are $\approx 15\lambda_{Db} = 3\,\mathrm{mm}$ wide. So the potential builds up as expected with a constant plasma potential in the bulk region and equal sheaths to the grounded boundaries.

 Looking at the densities (s. figure (5.3)) one can see that the densities are not equally distributed around the axis nr=0. Instead their maximum is at nr ≈ 40. In three dimensions this leads to a torus form. The particle density distributions are close to other simulated results [20], but further studies of micro discharges are not of interest in this thesis.

5.2 Simulation of an asymmetric ccrf discharge

A bigger domain size (500x200), which gets closer to the experimental size, is used from now on. In the following simulations with an asymmetry factor of 0.6 will be used, resulting in a cathode radius of $\approx 2.5\,\mathrm{cm}$. In figure (5.4) the averaged potential is shown. Due to the asymmetry a negative self-bias voltage at the cathode builds up. This is a main difference to one-dimensional simulations. To compare the potential with one-dimensional simulations (s. figure (2.6)) one has to look at the potential at the axis nr=0 (s. figure
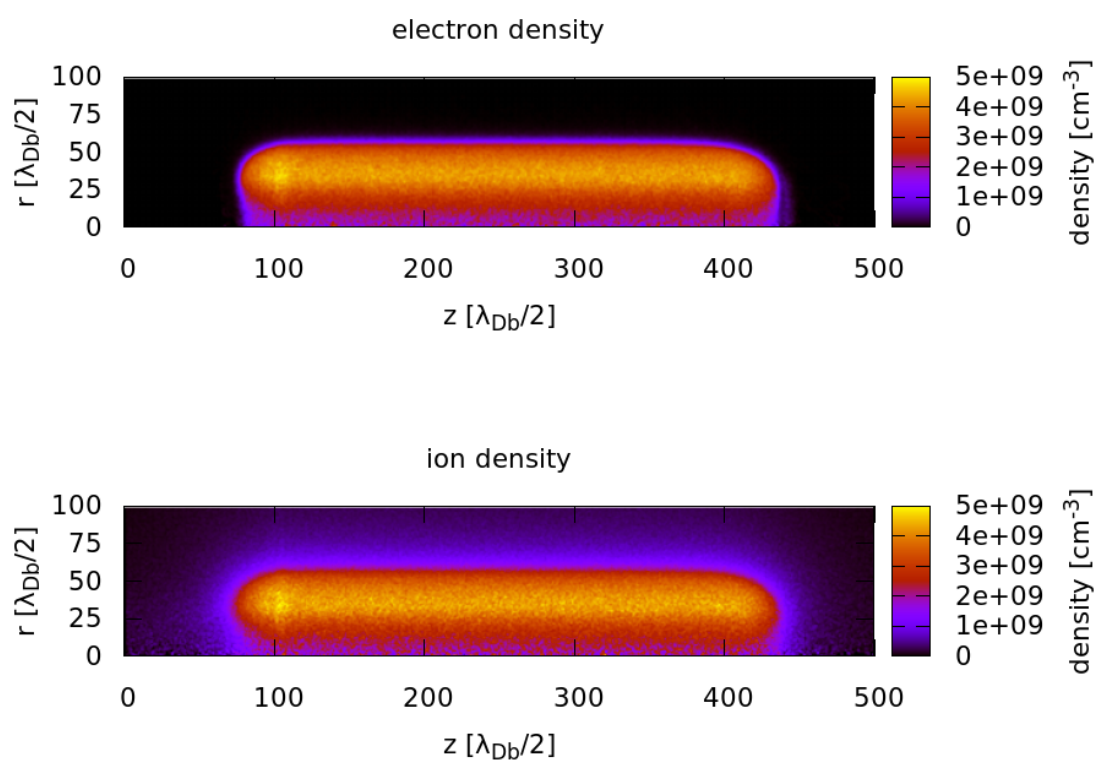
Figure 5.3: Charged particle density distribution with a micro cathode (radius of $r_{cathode} \approx$ 3 mm) with argon as working gas.

(5.5)). The shape is the same despite the self-bias voltage which shows the advantage of two-dimensional simulations to obtain a realistic potential.
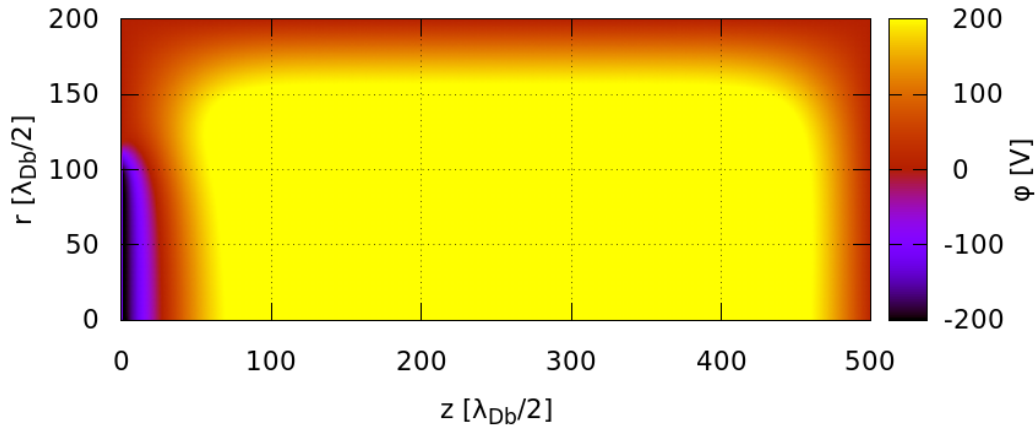
Figure 5.4: Potential of an argon rf discharge with an asymmetry ratio of 0.6. This leads to a cathode size of $r_{cathode} \approx 2.5\,\mathrm{cm}$. The pressure was set to $30\,\mathrm{Pa}$ and the power was $U_{rf} = 1000\,\mathrm{V_{pp}}$.

In figure (5.6) the electron and ion number density after a runtime of 30 rf cycles after initialization are shown. This is a not yet fully equilibrated state of the plasma, due to the long run-times. One can see that the bulk region is slightly deformed at the cathode side. This is due to the self-bias voltage which leads to a reduced electron flux towards the cathode. The ions follow the motion of the electrons. The density distributions show the expected behavior of a central quasi-neutral plasma and typical sheath structures as discussed in chapter 2.

Now the density distribution can be compared with the previous one-dimensional results. Therefore, the number density distributions of the charged species at the axis (s. figure (5.8)) are taken, which equals the one-dimensional domain.

One can see the quasi-neutral bulk region and the ion flux towards the walls. There is a higher flux of ions towards the cathode than to the anode due to the self-bias voltage. This additional flux is not covered by the one-dimensional simulation. Additionally, the cathode sheath is larger in two dimensions, due to the self-bias voltage. So in a one-dimensional simulation the total ion flux towards the cathode and the cathode sheath width are slightly underestimated. Nevertheless, the form of the number density distributions is nearly the same, which shows that a one-dimensional simulation is a good approximation regarding the number densities for capacitively discharges near the center.
In addition to the density distributions and the potential a closer look at the energy distributions of the plasma particles is taken. The ion energy distributions in r and z direction
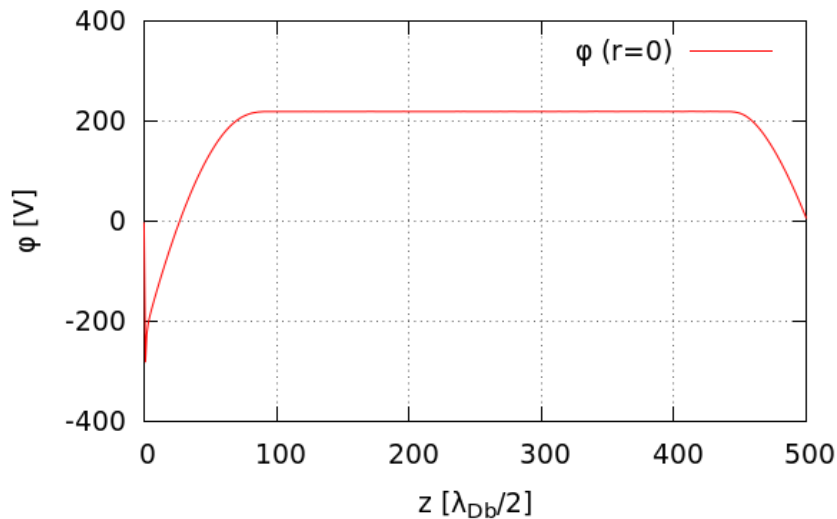
Figure 5.5: Potential of an argon discharge at the axis ($r = 0$).

are located in the appendix (7.1) and (7.2). The z component of the ion energy distribution shows the expected behavior of cold ions in the bulk and accelerating ions towards the electrodes (s. figure (7.1 (a))), when averaged along r at fixed z. The radial component of the ion energy distribution (s. figure (7.2)) shows the same acceleration of the ions towards the wall. Near the cathode edge (r=120) the ions are accelerated towards the cathode due to the radial potential gradient, which results in a larger ion energy.

When comparing the electron energy distributions with the results from the one dimensional PIC simulation (s. figure (3.4)), one can see that for the z component of the electron energy distribution (s. figure (7.3 (a))) the shape of the distributions is nearly the same, except near the cathode. Due to the asymmetry the potential has additional radial gradients, especially above the cathode (s. figure (5.4)). This leads to a shift in the electron energy distribution function near the cathode, where the electrons get pushed in radial direction. In the experiment the cathode usually is not located at the wall, but stands in free space. Here the cathode is embedded in a grounded ring. So this is an effect which can be modified by moving the cathode into the domain. Then the mesh and the boundary conditions have to be applied accordingly. But I am not doing this approach in this thesis. Naturally, the r component of the electron distribution function is affected by the same radial gradient of the potential and builds up an analogue distribution function (s. figure (7.4)).

The two-dimensional model can now be used to test some of the assumptions applied for the analyisis of the distribution functions for negative oxygen ions in the previous chapter. Since an ordinary argon plasma does not contain negative ions, the former model of SIE is artificially applied to clarify some basic physics mechanisms. The injected anions are treated as negatively charged argon ions which do not collide with other particles. In the one-dimensional model, the argument was used that injected anions should have enough energy to cross the sheath in front of the anode, due to the additional energy from the self-bias voltage.
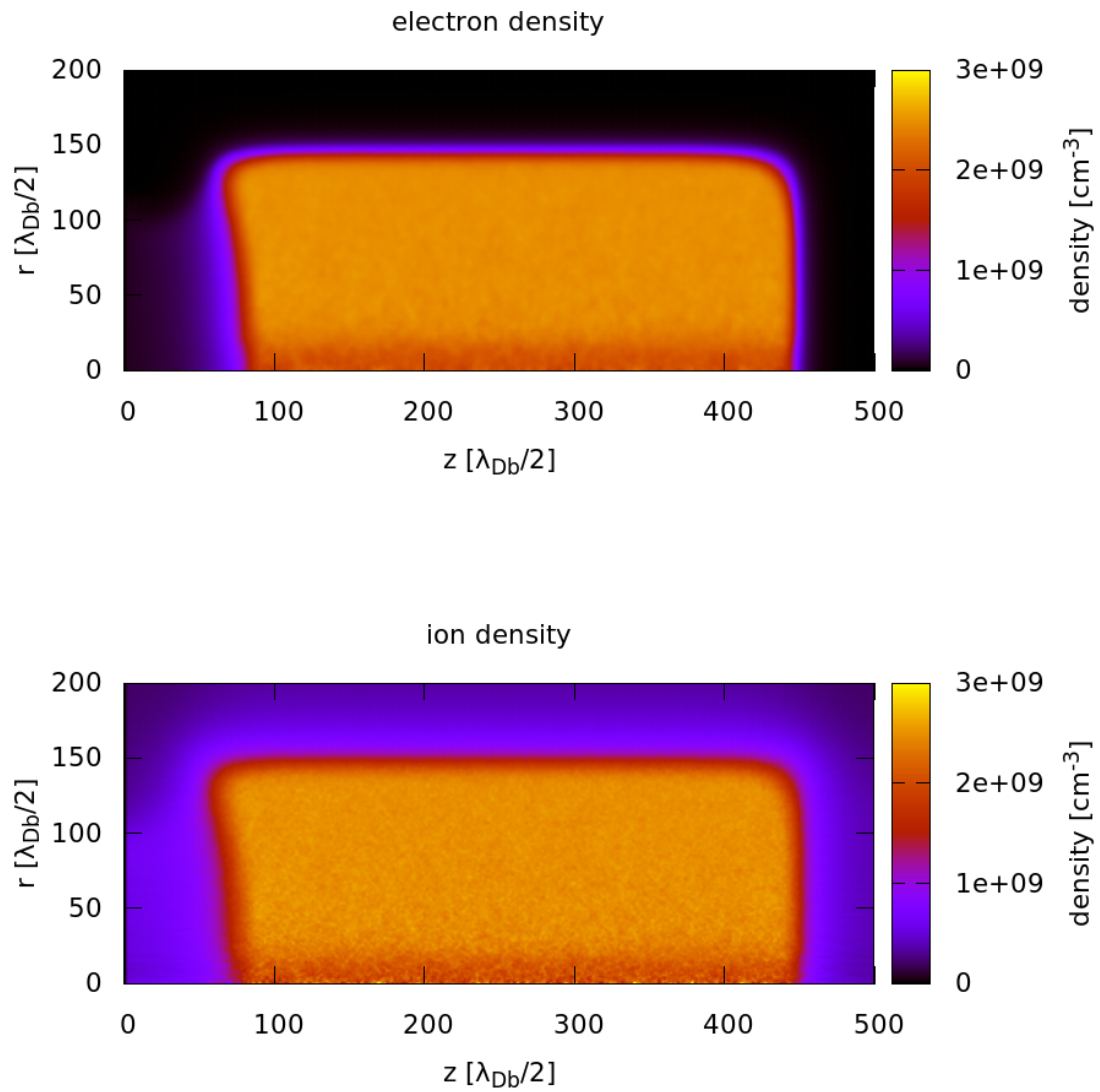
Figure 5.6: Charged particle density distribution of an argon discharge.
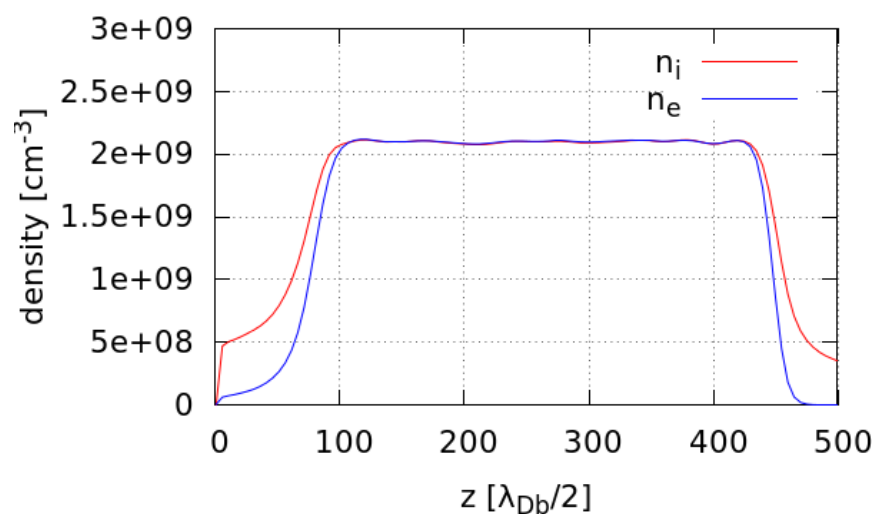
Figure 5.7: Charged particle density distribution of an argon discharge at the center of the discharge from a two-dimensional PIC simulation at $30\,\mathrm{Pa}$ and $1000\,\mathrm{V_{pp}}$.
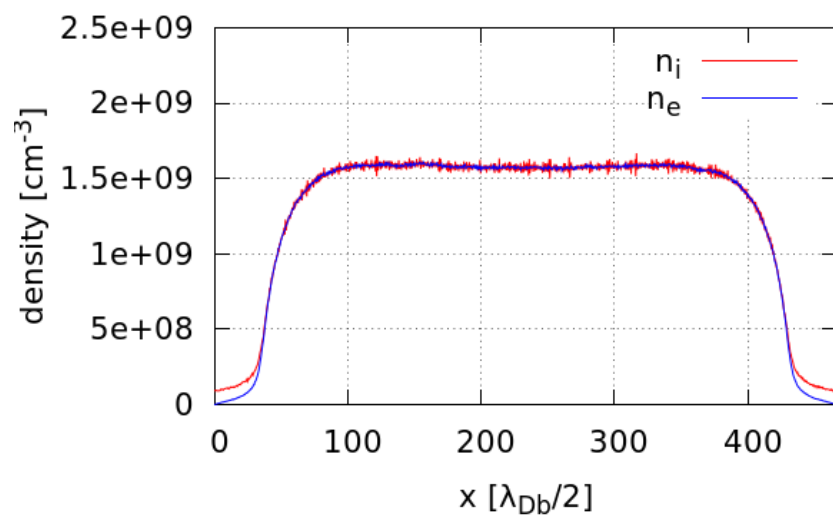
Figure 5.8: Charged particle density distribution of an argon discharge out of an one-dimensional PIC simulation at $30\,\mathrm{Pa}$ and $400\,\mathrm{V_{pp}}$.
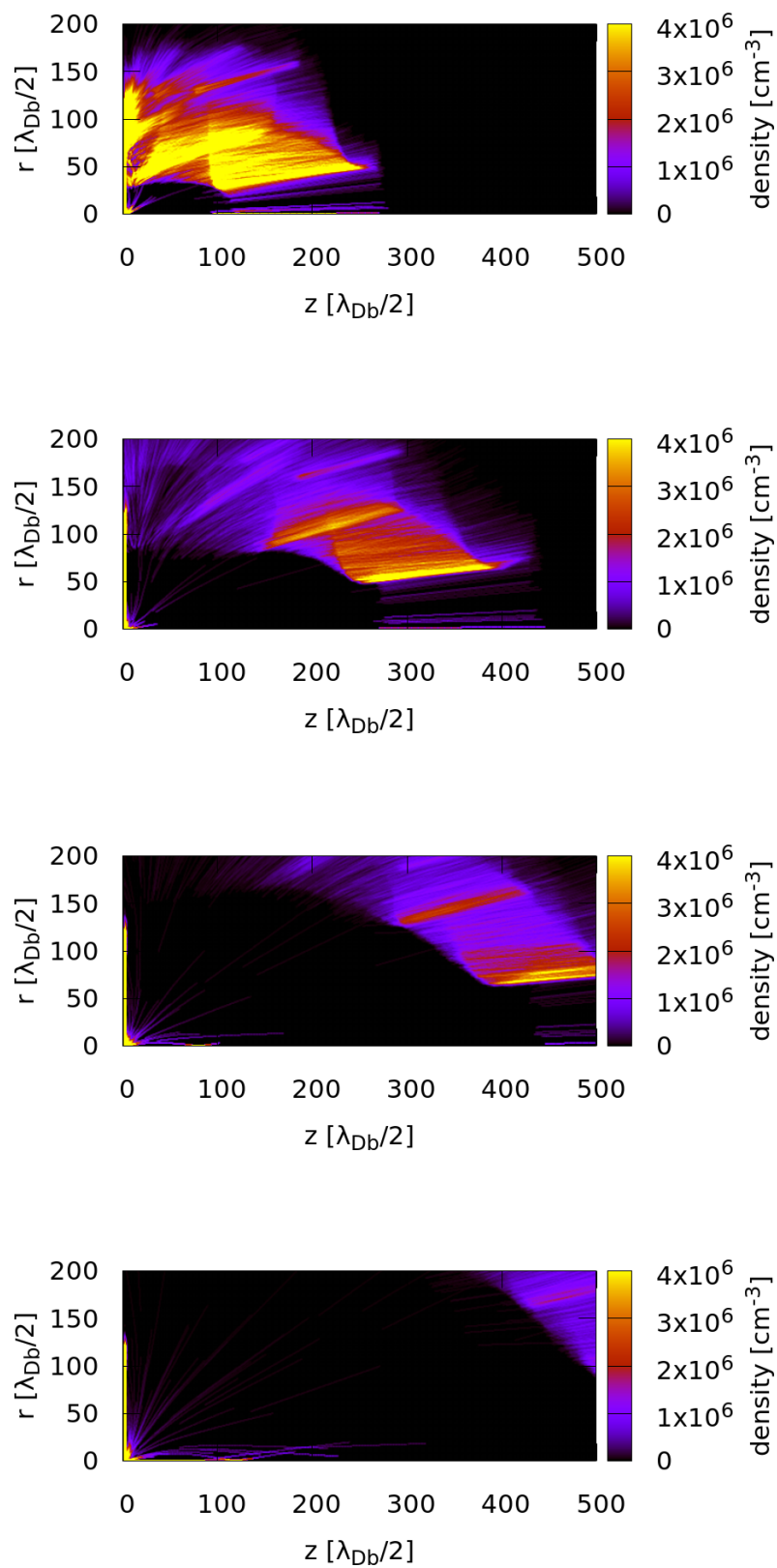
Figure 5.9: Time evolution of the surface anion number density distribution.

The results of the two-dimensional model can be used to study the behavior of surface anions. In the case of an argon discharge with artificially produced surafce anions there is no other contribution from volume processes for the generation of negative ions. Therefore the analysis of effects on the distribution of negative ions is straight forward without the need for separation of the volume and surface species. The resulting evolution of the number density distribution of the anions in an argon ccrf discharge is shown in figure (5.9). One can see that the anions are accelerated in the sheath and after they cross the domain impinge on the anode and on the wall, since their energy is higher than the potential drop of the sheaths. The energy distribution of the anions also shows that the high-energy anions fly only towards the anode where they are absorbed. This verifies the former assumptions made in the one-dimensional analysis (see chapter 4). In the two-dimensional case the low-energy peak in the energy distribution function of the negative ions disappears due to the effect mentioned before and the modelling gets very close to the experiment.

6 Conclusions

In this thesis I successfully simulated electronegative capacitively coupled rf plasmas under low pressure oxygen using the Particle-in-Cell method. The first step was the use of one dimensional models. Due to latest experimental results, showing a high-energy peak in the anion energy distribution depending on the used cathode material, secondary ion emission effects were also implemented into the PIC wall model. Since a detailed understanding theoretical understanding of such processes is still missing, an injection coefficient proportional to the number of impinging ions was implemented. With this model I was able to reproduce qualitatively the experimental measured high-energy peak of negative oxygen ions O^- at the anode. The simulation results yielded an additional low-energy peak in contradiction to the experiment. It could be shown that the peak forms due to the surface anions staying in the discharge and then colliding with neutrals in the sheaths. Varying the system parameters a better understanding of the dependence of the anion energy distribution function with respect to applied power, pressure and injection ratio η was obtained. The results were very close to the experimental measurements except for the variation of the injection parameter η, which only slightly affected the resulting anion energy distributions. It was shown that due to the lack of asymmetry, which cannot be covered in an one-dimensional simulation, the injected anions stay in the discharge and then add up to a constant density background, nearly independent of the different chosen injection ratios η. In contrast the experiment shows big differences for different cathode materials.

To overcome the shortcomings of the one-dimensional model, a two-dimensional model was introduced. With this two-dimensional model a micro discharge and an asymmetric ccrf discharge with argon as a working gas have been simulated. Especially, the influence of the asymmetry on the number density distribution and on the energy distribution could be observed. It was confirmed that the one-dimensional model is a good approximation for the center of the discharge, except for the forming of a self-bias voltage. To prove the assumptions made in the one-dimensional simulation regarding the negative anions, SIE was implemented in the tow-dimensional model, too. The self-bias voltage leads to a higher energy of the injected anions. It was shown that they impinge on the anode, where they are absorbed. This explains the discrepancy between the former one-dimensional model, where an additional low-energy peak appeared, and the experiment, where this feature is missing. The absorption in the two-dimensional model removes this low-energy peak in the simulation. Due to runtime limits only proof-of-principle studies were possible.

To the best of my knowledge until now there do not exist any publications of two dimensional PIC simulations of low temperature laboratory plasmas yet. In future work the next step would be to implement oxygen as a working gas and apply physically motivated SIE in the two dimensional model. Then, one could apply different cathode materials to see the influence of different work functions on the anion O^- energy distribution function, which could not be obtained in one dimension. So the developed tool has still a lot of potential.

7 Appendix

7.1 Energy distributions

In the following the energy distributions of electrons and ions from a two-dimensional PIC simulation in an asymmetric ccrf discharge are shown. For the description and interpretation I refer to chapter (5).
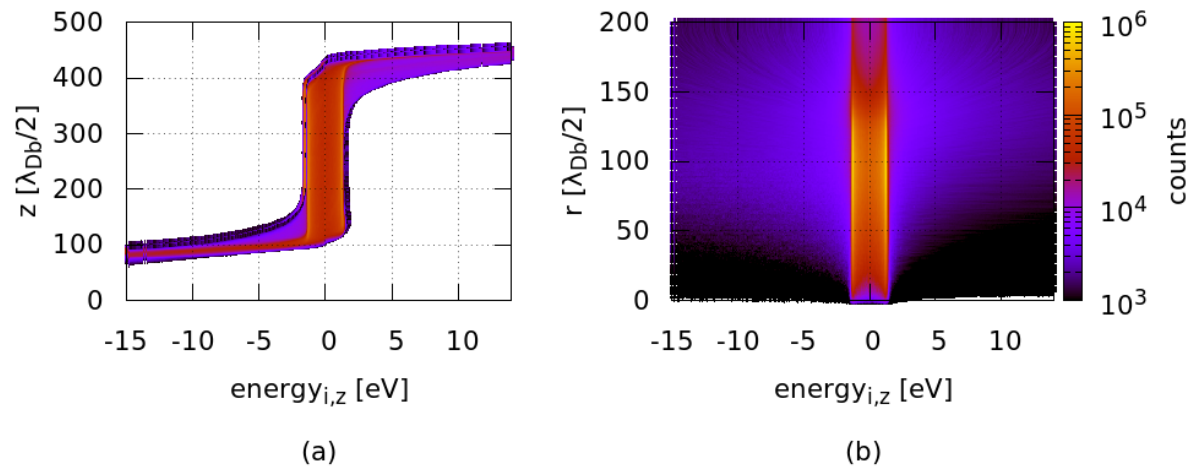
Figure 7.1: Ion energy distribution in z direction. (a) shows the averaged energy resolved for the vertical z axis and (b) for the radial r axis.
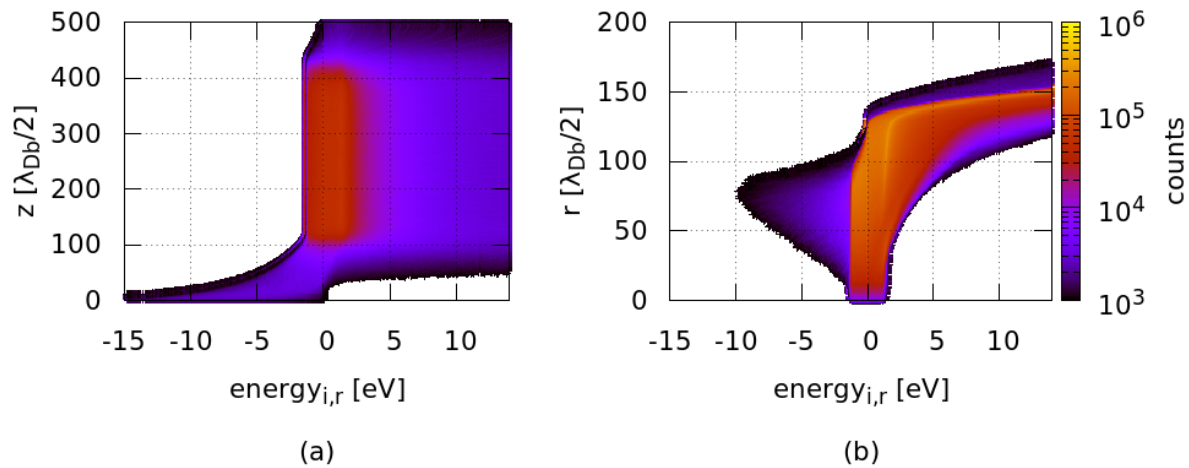
Figure 7.2: Ion energy distribution in r direction. (a) shows the averaged energy resolved for the vertical z axis and (b) for the radial r axis.
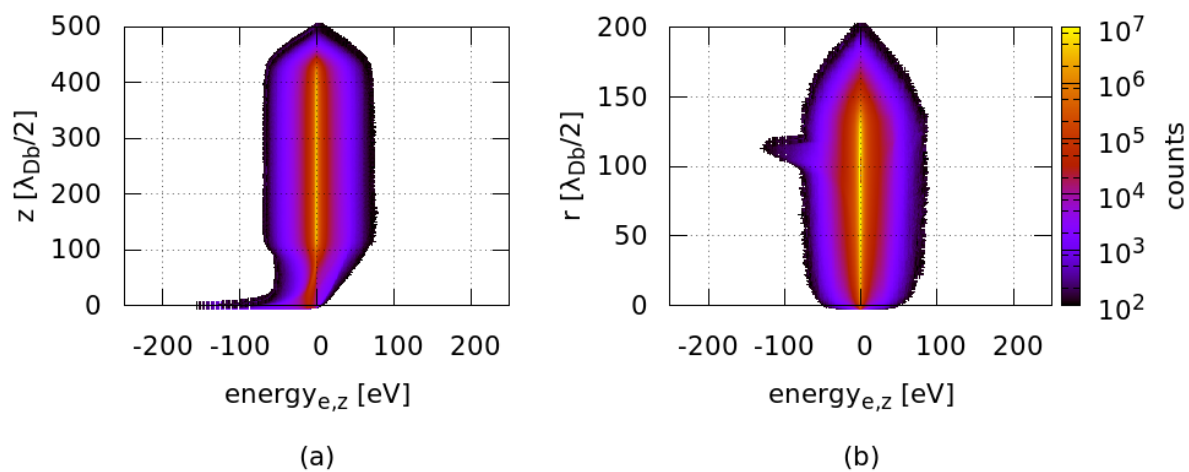
Figure 7.3: Electron energy distribution in z direction. (a) shows the averaged energy resolved for the vertical z axis and (b) for the radial r axis.
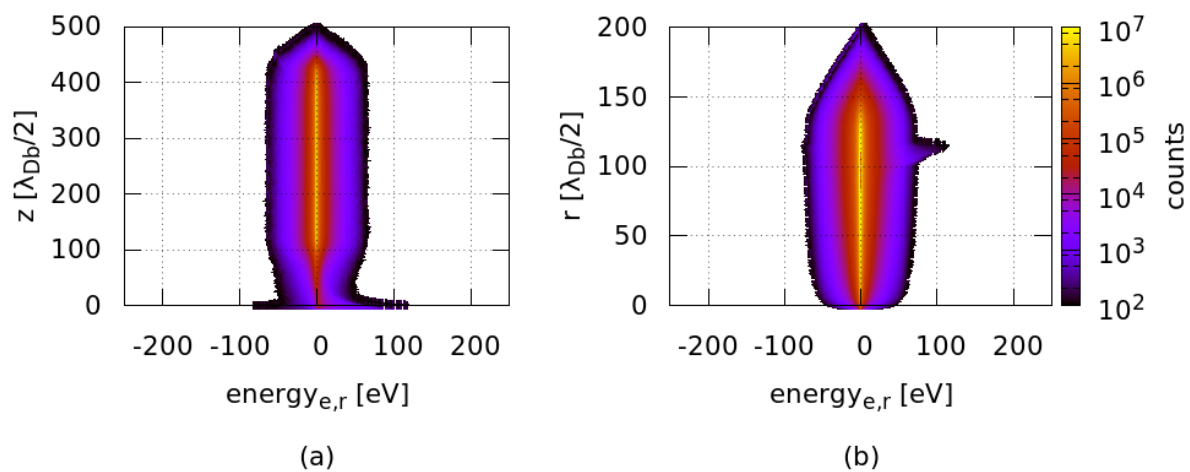
Figure 7.4: Electron energy distribution in r direction. (a) shows the averaged energy resolved for the vertical z axis and (b) for the radial r axis.

List of Figures

Bibliography

[1]   U. Cvelbar, M. Mozetic, and M. Klansjek-Gunde. "Selective oxygen plasma etchin of coatings". In: *Plasma Science, IEEE* 3.2 (2005), pp. 236–237.

[2]   M. Zeuner et al. "Sputter process diagnostics by negative ions". In: *Journal of Applied Physics* 83.10 (1998), pp. 5083–5086.

[3]   J. Meichnser et al. "Nonthermal Plasma Chemistry and Physics". In: (2013).

[4]   S. Scheuer. "Plasmadiagnostische Untersuchungen zur Charakterisierung von Moden in elektronegativen RF-Plasmen". In: *Master thesis* (2015).

[5]   D. Tskhakaya et al. "The Particle-In-Cell Method". In: *Contrib. Plasma Phys.* 47.8-9 (2007), pp. 563–594.

[6]   J. Duras. "Instabilities in ion thrusters by plasma-wall interactions". In: *Diplom Thesis* (2011).

[7]   H. Kawano and F. M. Page. "Experimental methods and techniques for negative-ion production ionization". In: *International Journal of Mass Spectrometry and Ion Physics* 50 (1983), pp. 1–33.

[8]   R. Breitwieser and W. Rush. "Saha-Langmuir Surface Ionization Relation". In: *NASA Technical Memorandum* (1965).

[9]   I. Langmuir and K. H. Kingdon. "Thermionic Effects Caused by Vapours of Alkali Metals". In: *Proc. R. Soc.* 107 (1925), pp. 61–79.

[10]   S. Ustaze et al. "Electron Capture and Loss processes in the Interaction of Hydrogen, Oxygen and Fluorine Atoms and Negative Ions with a MgO(100) Surface". In: *Physical Review Letters* 79.18 (1997), pp. 3526–3529.

[11]   J. Los and J.J.C. Geerlings. "Charge exchange in atom-surface collisions". In: *Physic Reports* 190.3 (1990), pp. 133–190.

[12]   C. Kullig., J. Meichsner, and K. Dittmann. "Detachment-induced electron production in the early afterglow of pulsed cc-rf oxygen plasmas". In: *Physics of Plasmas* 19 (2012), pp. 73–100.

[13]   J. Meichsner, K. Dittmann, and C. Kullig. "Electron and Negative Ion Analysis in Oxygen Capacitively Coupled Radio Frequency Plasma". In: *Contrib. Plasma Phys.* 52.7 (2012), pp. 49–58.

[14]   C. K. Birdsall and A. B. Langdon. "Plasma Physics via Computer Simulations". In: (2004).

[15]   S. Li Xiayoe, J.R. Gilbert, and J.W. Demmel. "SuperLU Users' Guide". In: (1999).

[16]   J.P. Boris. "Relativistic plasma simulation-optimization of a hybrid code". In: *Proceedings of the 4th Conference on Numerical Simulation of Plasmas* (1970), pp. 3–67.

[17]   F.X. Bronold et al. "Radio-frequency discharges in oxygen: I. Particle-based modelling". In: *J. Phys. D: Appl. Phys.* 40 (2007), pp. 6583–6592.

[18]   V.V. Dimakopoulos, E. Leontiadis, and G. Tzoumas. "A portable C compiler for OmpenMP V.2.0". In: *Proc. EWOMP 2003, 5th European Workshop on OpemMP* (2003), pp. 5–11.

[19]   E. Kawamura et al. "Ion energy distribution in rf sheaths; review, analysis and simulation". In: *Plasma Sources Sci. Technol.* 8 (1999), R45–R64.

[20]   T. I. Farouk. "Modeling and Simulations of DC and RF Atmospheric Pressure Nonthermal Micro Plasma Discharges: Analysis and Applications". In: *Doctor Thesis* (2009).

Acknowledgments

I wish to thank the whole work group of Prof. Ralf Schneider, who put me in touch with this Master Thesis and helped me with good advice and support during this thesis.
They always had time to discuss current topics and to help me, no matter if it was about my thesis work or just for fun. A special thanks goes to Tabea Stegmaier which supported me morally and culinary especially during the last part of this thesis. Last but not least, thanks to my family who always backed me up no matter what and everyone else who supported me during this thesis.